

Modeling the microphysics of CO₂ ice clouds within wave-induced cold pockets in the martian mesosphere



C. Listowski^{a,*}, A. Määttänen^a, F. Montmessin^a, A. Spiga^b, F. Lefèvre^c

^a Université Versailles St-Quentin; Sorbonne Universités, UPMC Univ. Paris 06; CNRS/INSU, LATMOS-IPSL, 11 bd d'Alembert 78280 Guyancourt, France

^b Sorbonne Universités, UPMC Univ. Paris 06; CNRS/INSU, LMD-IPSL, 4 Place Jussieu, 75252 Paris Cedex 05, France

^c Sorbonne Universités, UPMC Univ. Paris 06; Université Versailles St-Quentin; CNRS/INSU, LATMOS-IPSL, 4 Place Jussieu, 75252 Paris Cedex 05, France

ARTICLE INFO

Article history:

Received 6 November 2013

Revised 14 March 2014

Accepted 16 April 2014

Available online 26 April 2014

Keyword:

Mars
Terrestrial planets
Mars, atmosphere
Atmospheres, dynamics

ABSTRACT

Mesospheric CO₂ ice clouds on Mars are simulated with a 1D microphysical model, which includes a crystal growth rate adapted to high supersaturations encountered in the martian mesosphere. Observational constraints (crystal radius and opacity) exist for these clouds observed during the day around the equator at ~60–80 km altitude. Nighttime mesospheric clouds interpreted as CO₂ ice clouds have also been characterized at low southern latitudes, at ~90–100 km altitude. From modeling and observational evidence, it is believed that mesospheric clouds are formed within temperature minima created by thermal tides, where gravity wave propagation allows for the creation of supersaturated layers (cold pockets). Thus, temperature profiles perturbed by gravity waves are used in the model to initiate nucleation and maintain growth of CO₂ ice crystals. We show that it is possible to reproduce the observed effective radii for daytime and nighttime clouds. Crystal sizes are mainly governed by the altitude where the cloud forms, and by the amplitude of supersaturation. The temporal and spatial behavior of the cloud is controlled by the extent and lifetime of the cold pocket. The cloud evaporates fast after the cold pocket has vanished, implying a strong correlation between gravity wave activity and CO₂ cloud formation. Simulated opacities remain far below the observed ones as long as typical dust conditions are used. In the case of the lower daytime clouds, the enhanced mesospheric dust loading typically reached during dust storm conditions, allows for greater cloud opacities, close to observed values, by supplying the atmosphere with condensation nuclei. However, CO₂ ice clouds are not detected during the dust storm season, and, because of fast sedimentation of dust particles, an exogenous supply (meteoritic flux) appears necessary to explain opacities of both daytime and nighttime mesospheric CO₂ ice clouds along their whole period of observation.

© 2014 Elsevier Inc. All rights reserved.

1. Introduction

Since the first probable observation of a CO₂ mesospheric ice cloud on Mars (Clancy and Sandor, 1998), and the unambiguous spectral detection by Montmessin et al. (2007), a full theoretical addressing has been lacking about how the main component of the atmosphere (~95%) condenses to form CO₂ ice clouds in the mesosphere. Studies have mainly dealt with microphysical modeling of tropospheric CO₂ ice clouds appearing in the polar night (Wood, 1999; Tobie et al., 2003; Colaprete et al., 2003, 2008).

Numerous observations of mesospheric clouds have been carried out by several instruments (Clancy et al., 2003, 2007; Montmessin et al., 2006, 2007; Scholten et al., 2010; Määttänen

et al., 2010; McConnochie et al., 2010; Vincendon et al., 2011; Sefton-Nash et al., 2013). Daytime clouds could only be identified as CO₂ ice clouds by OMEGA thanks to the spectral 4.26 μm signature (Montmessin et al., 2007; Määttänen et al., 2010; Vincendon et al., 2011), and by CRISM, which allowed to indirectly identify CO₂ clouds by spectroscopically ruling out the possibility of water ice or dust composition (Vincendon et al., 2011). Both instruments observed mean effective radii around 0.5–3 μm and opacities are around ~0.1 at altitudes ranging between 60 km and 85 km. Night clouds were indirectly identified as CO₂ ice clouds thanks to concomitant detection by stellar occultation of detached aerosol layers and temperatures below the condensation point of CO₂ (Montmessin et al., 2006). Effective radii range between 80 and 130 nm, opacities around 0.01 at 200 nm. The top of the detached layers were systematically found below or just at the lower part of the supersaturated area. The reason can be that the crystals

* Corresponding author.

E-mail address: constantino.listowski@latmos.ipsl.fr (C. Listowski).

Table 1

General characteristics of CO₂ clouds detected in the martian mesosphere with SPICAM (Montmessin et al., 2006), OMEGA (Määttänen et al., 2010) and CRISM (Vincendon et al., 2011). Opacities were measured at 200 nm (SPICAM, range of measured opacities: 0.006–0.05), 1 μm (OMEGA, range: 0.01–0.5), and 500 nm (CRISM). In SPICAM retrievals, errors in r_{eff} are ± 0.02 μm, and less than 1% in cloud opacity (see Table 1 and Fig. 4 of Montmessin et al., 2006). With OMEGA data, retrieval technique leads to errors in r_{eff} of 10% while much less in opacity (2%). In CRISM retrievals errors in r_{eff} and τ should be respectively $\sim 30\%$ and $\sim 20\%$ at maximum (see legend of Fig. 3 in Vincendon et al., 2011).

Instrument	LT	Altitude (km)	r_{eff} (μm)	τ
SPICAM	Night	~90–100	0.080–0.130	~0.01
OMEGA	Day	~60–80	1–3	<0.5
CRISM	Day	~60–80	0.5–2	<0.3

sedimented in sub-saturated environment before evaporation (Montmessin et al., 2006). It was also suggested that these crystals could rather be made of water ice (Vincendon et al., 2011). Table 1 summarizes the two main categories of (day/night) clouds with their average properties as reported from observations (errors associated with retrievals are also given).

Colaprete et al. (2008) made the first and only attempt to model with a martian GCM the formation of mesospheric clouds up to altitudes 60–70 km. While the observed opacities were obtained, modeled clouds were produced mainly at altitudes ~60–70 km with crystals effective radii in the range 1–10 μm, close to although larger than the typical radii derived from observations. Furthermore, discrepancies remain between the model and the observations regarding the spatial and seasonal distributions (González-Galindo et al., 2011).

The causes of the formation of CO₂ ice clouds in the mesosphere could be partly constrained from various observations and modeling results. First, temperatures well below the CO₂ condensation point in the mesosphere have been reported by the SPICAM instrument through stellar occultations, which suggests a strong potential for triggering CO₂ ice nucleation in an extremely supersaturated environment (Montmessin et al., 2006, 2011; Forget et al., 2009). An excursion below the condensation point of CO₂ of ~10 K at 80 km altitude was measured by Schofield et al. (1997) with the Mars Pathfinder entry descent and landing experiment at night. For a 95% composition in CO₂, this corresponds to a saturation ratio of ~10. Forget et al. (2009) have reported values of temperatures corresponding to saturation ratios S up to ~1000, around the mesopause at night (~100–120 km). Montmessin et al. (2011) also reported such extremely cold pockets as a frequent phenomenon, mostly without observing any systematic concomitant aerosol detached layer. It could either suggest that CO₂ condensation has not occurred, or that condensation has occurred but the cloud has already evaporated at lower altitudes, or that the cloud was too thin to be detected. Possibly the reason is that no condensation nuclei were present at these altitudes to trigger the phase change.

Homogeneous nucleation is excluded because of the very high required critical saturation ratios (S_{crit}). At 0.01 Pa, i.e. ~90 km, S_{crit} for homogeneous nucleation is $\sim 10^{15}$, which corresponds to ~50 K below the CO₂ condensation temperature: such temperatures have never been reported in Mars atmosphere. The largest saturation ratios expected above 100 km altitude range between 10^3 and 10^4 , according to temperature measurements in the high mesosphere (Forget et al., 2009; Montmessin et al., 2011). Heterogeneous nucleation is considered as the most probable mechanism for the onset of CO₂ ice crystal growth (see also Määttänen et al. (2005) for near surface conditions and Määttänen et al. (2010) for mesospheric conditions).

A recent modeling study shows that thermal tides are important for CO₂ cloud formation and that temperature minima predicted in the mesosphere are correlated with the observations of mesospheric

clouds (González-Galindo et al., 2011). Nevertheless, an additional mechanism appears required to obtain temperatures below the condensation point. Mesoscale processes, such as gravity waves, are known to be responsible for Polar Stratospheric Clouds (PSCs) on Earth (see e.g. Noel and Pitts, 2012) as well as for Polar Mesospheric Clouds (PMCs) (see e.g. Thomas, 1991; Rapp and Thomas, 2006). PMCs are considered as the closest counterparts to martian mesospheric clouds (Määttänen et al., 2013). Modeling showed that locations where gravity waves are most likely able to propagate up to the mesosphere are correlated with locations of CO₂ ice cloud observations (Spiga et al., 2012). These elements give motivation to model the formation of CO₂ clouds within a single-column full microphysical model (1D model), by creating highly supersaturated cold pockets caused by gravity waves. In doing so we follow the scenario already suggested by Clancy and Sandor (1998): “As a result CO₂ ice clouds should form within the temperature minima of tidal and gravity waves in the Mars mesosphere, and be fairly common phenomena at low-to-mid latitudes during day and night times.”

The purpose of this paper is to reproduce for the first time the effective radii and opacities observed (Table 1) by modeling the detailed processes responsible for the formation of mesospheric CO₂ ice clouds within wave-induced realistic cold pockets. We first introduce the full microphysical scheme in Section 2. The main inputs to our 1D model with a first sensitivity test of CO₂ ice condensation are described in Section 3. We then investigate in Section 4 the characteristics of clouds forming within cold pockets associated with gravity waves. We discuss these results in a wider perspective in Section 5 and we conclude in Section 6.

2. Physical principles and their formulation in the model

2.1. Microphysical processes

Our model includes the following processes: vertical transport (sedimentation and vertical mixing), nucleation and condensation/evaporation. A hybrid radius grid is used to avoid numerical diffusion (Jacobson et al., 1994). The radius of any CN (Condensation Nuclei) which would be involved as a substrate for nucleation is kept in memory. Thus, when the crystal evaporates, the original size of the CN is recovered. The radius grid extends from 1 nm to 100 μm. The core of the microphysical model is taken from a previous work on microphysics of H₂O ice clouds (Montmessin et al., 2002), and adapted to CO₂ clouds forming in the gas mixture CO₂/N₂ (proportions are 95% and 5% following Wood, 1999; Colaprete and Toon, 2003; Colaprete et al., 2008). Our model extends up to ~120 km altitude above the surface (with layer depth $dz \sim 2$ km), in order to encompass the altitudes of clouds monitored by SPICAM (Montmessin et al., 2006). Vertical transport is implemented according to the numerical scheme of Toon et al. (1989), where sedimentation is corrected to account for atmospheric vertical mixing represented by an eddy diffusion coefficient k_d . The condensable vapor (CO₂) is mixed through vertical mixing as well. Vertical mixing (eddy diffusion) is a simplified way of accounting for atmospheric dynamics (e.g. convection, waves) which participates to the transport of aerosols and gases. The coefficient k_d is determined from measurements (e.g. Chassefiere et al., 1992; Korabiev et al., 1993; Blamont and Chassefiere, 1993; Rodin et al., 1997). We use two values of k_d , $100 \text{ m}^2 \text{ s}^{-1}$ and $1000 \text{ m}^2 \text{ s}^{-1}$ in our model, following the average values expected in the troposphere/low mesosphere and mid/high mesosphere (as summarized in Izakov, 2007).

The Stokes fall velocity of particles is corrected by the Cunningham factor to account for low martian atmospheric densities (as in Montmessin et al., 2002) so that the sedimentation velocity is:

$$v_{\text{sed}} = v_{\text{Stokes}} \times C_c, \quad (1)$$

with v_{Stokes} the fall velocity in continuum regime and C_c the Cunningham factor accounting for the transition to free molecular regime.

$$v_{Stokes} = \frac{2}{9} \frac{\rho_d g a^2}{\eta} \quad (2)$$

$$C_c = 1 + Kn[1.246 + 0.42 \exp(-0.87/Kn)],$$

where ρ_d is the dust density (taken here as 2500 kg m^{-3}) and Kn is the Knudsen number, defined as the ratio of atmospheric mean free path over particle radius a .

We adopt Classical Nucleation Theory (CNT) assuming that nucleation is exclusively heterogeneous, as it is probably the case on Mars, for surface as well as for mesospheric conditions (Määttänen et al., 2005, 2010). Nucleation describes the energy needed to form a critical cluster (aggregate of molecules), which is responsible for subsequent phase change by its spontaneous growth. This energy barrier arises from the creation of a new interface between the condensed phase and the mother phase. The dynamics of heterogeneous nucleation is described by a nucleation rate (e.g. Keese, 1989; Määttänen et al., 2005):

$$J_{het} = Z_{het} \beta_{het} c_{surf} \exp(-\Delta F_{het}^*/kT), \quad (3)$$

where J_{het} is the heterogeneous nucleation rate per unit of (substrates) area ($\text{m}^{-2} \text{ s}^{-1}$), Z is the Zeldovich factor (as in Vehkamäki et al., 2007), β_{het} is the collision rate of adsorbed molecules (on the substrate) with the critical embryo, c_{surf} is the number concentration of molecules of the condensable vapor per unit area of substrate, ΔF_{het}^* the free energy of formation for the critical cluster, k the Boltzmann constant and T the background temperature (see Määttänen et al. (2005) for the expression of each coefficient). The contact parameter needed in ΔF_{het}^* is $m = 0.952$ (experimentally determined by Glandorf et al. (2002)). Contrary to Colaprete et al. (2008) we do not account for non-isothermal effects through a multiplying factor f_T in Eq. (3), which accounts for the heat release due to phase change of molecules, and so the subsequent reduction of nucleation efficiency (particularly when the major atmospheric component condenses). Indeed, CNT assumes nucleation is an isothermal process and f_T was derived by Feder et al. (1966) for homogeneous nucleation. However, in case of heterogeneous nucleation, the substrate efficiently thermalizes the cluster and evacuates the released heat (Määttänen et al., 2007). The non-isothermal coefficient would be needed in case of homogeneous nucleation, or for ion-induced nucleation, or also if the CN is much smaller than the critical embryo.

The nucleation probability (see e.g. Lazaridis et al., 1992) accounts for the fraction of dust particles which is activated:

$$P_{het}(R) = 1 - \exp(-4\pi R^2 J_{het} \Delta t), \quad (4)$$

where R is the CN radius, Δt the time interval considered for activation, here the time step dt of the model. Nucleation has the shortest characteristic time among all processes (sedimentation, vertical mixing, condensation/evaporation) in our simulations. The time step is fixed at $dt = 1 \text{ s}$; below this value, no significant modifications of simulation results appear. It is the characteristic time ($\sim 1/4\pi R^2 J_{het}$) over which nucleation is efficient enough to have $P_{het} > 0.5$.

For a concentration $n(R)$ of CN of radius R , and given $P_{het}(R)$, $P_{het}(R) \times n(R)$ gives the amount of activated CN of radius R . The formulation of activation in terms of probability implies that whatever the CN radius is, it can theoretically become activated if enough time is given (provided the environment remains supersaturated), thereby accounting for the stochastic nature of nucleation. Fig. 1 shows the nucleation probability in relation to the saturation ratio for different CN radii R . An abrupt increase in probability, from 0 to 1, occurs around what is called the critical

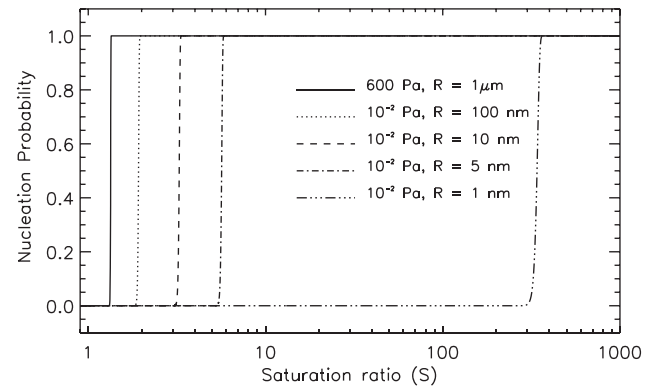


Fig. 1. Heterogeneous nucleation probabilities of CO_2 ice (given by Eq. 4) as a function of saturation ratio S , for various dust nuclei and two atmospheric pressures on Mars. The pressure 600 Pa is typical for average surface conditions, while 10^{-2} Pa is related to mesospheric conditions ($\sim 80\text{--}90 \text{ km}$).

saturation ratio, S_c , i.e. the saturation ratio needed to ensure an efficient activation of the CN of radius R ($S = S_c$ where $P_{het}(R) = 50\%$). The smaller the CN and lower the atmospheric density, the higher the critical saturation ratio. For mesospheric pressures (e.g. 0.01 Pa, $\sim 80\text{--}90 \text{ km}$ altitude) a 1 nm particle would need $S \sim 350$ (i.e. $\sim 15 \text{ K}$ below CO_2 condensation temperature) to be activated, while only $S \sim 3$ (i.e. $\sim 3 \text{ K}$ below condensation temperature) is needed for a 10 nm particle.

Ion-induced nucleation is ruled out, following Wood (1999). Estimation of maximum gaseous ion concentration from modeling studies (in absence of any ion concentration measurements except the Viking data above 100 km, from Hanson et al. (1977)) for the day and night ionosphere of Mars (respectively Molina-Cuberos et al., 2002; Haider et al., 2007), and also metallic ion concentrations from meteoroid ablation model coupled to ionospheric chemistry (Molina-Cuberos et al., 2003), have given the same peak values of ion concentration ($\sim 10^{10} \text{ m}^{-3}$). According to our estimations, using $f_T = 0.01$ (Määttänen et al., 2005), at $p \sim 0.01 \text{ Pa}$ ($\sim 90 \text{ km}$) ion-induced nucleation would start to be efficient for $S > 1000$. Saturation ratios of this order of magnitude are typically encountered at higher altitudes ($> 100 \text{ km}$, Forget et al., 2009; Montmessin et al., 2011). Heterogeneous nucleation can be triggered at much lower saturation ratios (Fig. 1). Thus, we do not consider ion-nucleation as a possible competitor for heterogeneous nucleation. It could start to compete for ion species with a charge $q \geq 3$ which are of minor importance in the atmosphere (models only consider single-charged species in the ionosphere, see e.g. Molina-Cuberos et al., 2002; Haider et al., 2007).

Once activated the dust particle hosts a subsequently growing/evaporating phase of ice. Condensation and evaporation processes of CO_2 crystals rely on the growth rate model called the CLASSIC model and described in Listowski et al. (2013). It is theoretically adapted to a near-pure vapor condensation with high supersaturations as encountered in the martian mesosphere, where temperature differences between the crystal surface and the environment are large. Growth rate models traditionally used for condensation of trace gases cannot be used because they are linearized in terms of this temperature difference; the CLASSIC model is a non-linearized growth model. Section 4.2 is dedicated to highlighting the differences in our modeling results between a trace-gas (linearized) growth model and our CLASSIC (non-linearized) model. As explained in Listowski et al. (2013), since no explicit formulation of the growth rate can be derived, an iterative method (e.g. Newton–Raphson algorithm) is needed to determine the growth rate of CO_2 crystals.

Crystals are considered spherical. The shape of a CO_2 ice crystal is far from a simple sphere as suggested by experiments (Foster et al.,

1998) and theoretical studies (Wood, 1999), from which one expects shapes close to octahedrons. The shape of a crystal is closely linked to surface kinetics processes occurring during the growth process (e.g. Wood et al., 2001; Bailey and Hallett, 2004). Indeed, surface kinetics impacts (limits) the efficiency of vapor molecules integration into the crystal lattice, which may vary from one crystal face to another, leading to a particular crystal shape and impacting the overall growth rate. An alternative to the accurate modeling of these processes (e.g. Wood et al., 2001) is the use of a multiplying factor C in the growth rate, called capacitance, which depends on crystal size, shape, and atmospheric temperature (Bailey and Hallett, 2004). This coefficient requires a lot of observational and experimental constraints because its theoretical expression alone, which relies on electrostatic analogy, often fails (Bailey and Hallett, 2006). However, data allowing to constrain C for CO_2 ice crystals in martian conditions have never been published so far. Besides, comparison of Wood (1999)'s growth rate, which includes the modeling of surface kinetics, to CO_2 ice growth experiments (Glandorf et al., 2002) and to growth rate model ignoring surface kinetics effects (Colaprete et al., 2008) suggests that surface kinetics could (possibly) act for $S \leq 1.1$ (reducing the growth rate), the effect vanishing for larger S (see Fig. 5 of Colaprete and Toon, 2003). However, the experiment of Glandorf et al. (2002) does not allow to definitely conclude on the importance of surface kinetics effect in mesospheric conditions and large saturation ratios. In lack of any experimental evidence we ignore the possible influence of shape and surface kinetics on crystal growth, and remain with spherical crystals, our aim being to determine mean effective sizes of crystals.

In order to derive the growth rate, we first iteratively solve for the crystal surface temperature T_a , following the system of equations:

$$\begin{aligned} I_m &= -\frac{4\pi a M_v D}{RT_\infty} (p_{v,\infty} - p_{v,a}), \\ T_a &= T_\infty - \frac{L_{sub} I_m}{4\pi a K}, \\ p_{v,a} &= p_{sat}(T_\infty) S_{eq} \exp\left(\frac{L_{sub} M}{R} \frac{T_a - T_\infty}{T_\infty^2}\right), \end{aligned} \quad (5)$$

where I_m is the mass transfer rate (kg s^{-1}), $p_{v,\infty}$ the background partial pressure of vapor (CO_2), $p_{v,a}$ the partial pressure of vapor at the crystal surface, T_∞ the background atmospheric temperature, R the gas constant, and M_v the molar mass of the condensing vapor (CO_2 , 44.03 g mol^{-1}). The coefficients D and K are respectively the binary diffusion coefficient of CO_2 in N_2 and thermal conductivity of the gas mixture CO_2/N_2 (as given in Listowski et al., 2013). Transport coefficients are corrected according to Fuchs and Sutugin (1971) to account for transition ($0.1 \leq Kn \leq 100$) to free molecular regime ($Kn \gg 1$) that prevails on Mars. The pressure p_{sat} is the saturation vapor pressure of CO_2 (James et al., 1992), and L_{sub} the sublimation heat of CO_2 (as given in Listowski et al., 2013). The Kelvin factor S_{eq} accounts for curvature effects: $S_{eq} = \exp(2\sigma M_v / a \rho_{ice} RT_\infty)$, where σ and ρ_{ice} are respectively the surface energy (0.08 J m^{-2}) and density (1600 kg m^{-3}) of CO_2 ice (Wood, 1999). The Kelvin factor deviates from the unit value for radii $\leq 100 \text{ nm}$.

Combining the Eqs. (5), we solve for $f_c(T_a) = 0$ where:

$$f_c(T_a) = T_a + c_0 \exp(c_1 T_a) - c_2, \quad (6)$$

with:

$$\begin{aligned} c_0 &= \frac{M_v D p_{sat} L_{sub}}{RT_\infty K} S_{eq} \exp\left(\frac{-L_{sub} M_v}{RT_\infty}\right), \\ c_1 &= \frac{L_{sub} M_v}{RT_\infty^2}, \\ c_2 &= T_\infty + \frac{M_v D L_{sub}}{KRT_\infty} p_{v,\infty}. \end{aligned} \quad (7)$$

Having found T_a , one can then obtain the growth rate dr/dt , through the mass transfer rate I_m (< 0 in case of condensation) (Listowski et al., 2013):

$$\begin{aligned} \frac{dr}{dt} &= -\frac{1}{4\pi a^2 \rho_{ice}} I_m \\ &= -\frac{1}{4\pi a^2 \rho_{ice}} \frac{4\pi a K}{L_{sub}} (T_\infty - T_a) \end{aligned} \quad (8)$$

2.2. Adding radiative heat transfer in the crystal energy budget

Contrary to Listowski et al. (2013), we have included the influence of radiative heat transfer on the cloud crystals in the CLASSIC model, in a simple way, accounting for radiative cooling, solar heating, and atmospheric heating. The energy balance given by the second equation of the system (5) is modified as follows:

$$4\pi a K (T_a - T) + P_{cool}(a, T_a) = -L_{sub} I_m + P_{sol}(a) + P_{atm}(a), \quad (9)$$

where $P_{cool}(a, T_a)$, $P_{sol}(a)$, $P_{atm}(a)$ are the radiative cooling term of the crystal at a surface temperature T_a , the solar heating term and the atmospheric/surface IR heating term, respectively.

These three terms can be written in simple power-law forms through calculation and optimization detailed in Appendix A. The CO_2 ice optical constants are given by the most recent datasets of Hansen (1997, 2005), who heavily refined the original compilation of Warren (1986). The atmosphere-surface contribution $P_{atm}(a)$ relies on infrared flux to space as given by the Martian Climate Database (Millour et al., 2012), from which an equivalent black-body temperature is extracted. The three radiative terms can be written as follows:

$$P_{cool}(a, T_a) = k_c(T_a) a_{\mu m}^{z_c(T_a)} \quad (10)$$

$$P_{sol}(a) = k_s a_{\mu m}^{z_s} \quad (11)$$

$$P_{atm}(a) = k_a a_{\mu m}^{z_a}, \quad (12)$$

where $a_{\mu m}$ is the crystal radius in μm (expressions of $k_c(T_a)$, k_s , k_a , $z_c(T_a)$, z_s and z_a are given in Appendix A). $P_{cool}(a, T_a)$ has a simple expression which allows to build an analytical function from Eq. (9), to iteratively solve for T_a . P_{cool} derivative has also an analytical expression which can be easily included in the Newton–Raphson routine. The new function to iteratively solve for T_a is as follows:

$$f_{c,rad}(T_a) = T_a + c_0 \exp(c_1 T_a) + R_0 \exp[R_1(T_a)] - c_2 - R_1, \quad (13)$$

with:

$$\begin{aligned} R_0(T_a) &= \frac{k_c(T_a)}{4\pi a K} \\ R_1(T_a) &= z_c(T_a) \ln(a_{\mu m}) \\ R_2 &= \frac{k_s a_{\mu m}^{z_s} + k_a a_{\mu m}^{z_a}}{4\pi a K} \end{aligned} \quad (14)$$

2.3. Treatment of near-pure condensation: trace gas scheme

We work with a fixed pressure level grid, as it is done in the core of the 1D H_2O ice cloud model (Montmessin et al., 2002), from which we built our model for the CO_2/N_2 gas mixture. The condensation of the major atmospheric component questions this approach, because of possibly significant total pressure changes. However, we have evaluated its correctness. Let m_v be the mass of the vapor in a given atmospheric layer of the model and $m_{a,0}$ the mass of that layer. During evaporation/condensation, $m_a = m_{a,0} \pm dm_a$. The atmospheric mass m_a can be considered constant as long as $|dm_v| = |dm_a| \ll m_a$, where dm_v is the variation of vapor mass due to condensation. Let $q_v = m_v/m_a$ be the mass

mixing ratio of the vapor. In the case of a trace gas $dq_v \sim dm_v/m_a$ so that $|dm_v| \ll m_a$ is equivalent to $|dq_v| \ll 1$. In the case of CO₂ condensation on Mars, with CO₂ being the major component of the atmosphere, the variation of m_a has to be reconsidered. One needs to rewrite dq_v (with $dm_v = dm_a$): $dq_v = d[m_v/m_a]$ so that $dq_v \sim \frac{dm_v}{m_a}(1 - q_{v,0})$ where $q_{v,0} = m_{v,0}/m_{a,0}$ is the average mass mixing ratio. Thus:

$$\frac{|dm_v|}{m_a} \ll 1 \iff \frac{|dq_v|}{1 - q_{v,0}} \ll 1$$

For CO₂ on Mars, $q_{v,0} \sim 0.97$ (kg/kg) then: $|dm_v|/m_a \ll 1$ is equivalent to $(30 \times dq_v) \ll 1$. If we choose $\leq 1\%$ as a condition for $\ll 1$ we then have that $|dq_v|/(1 - q_{v,0}) \ll 1$ is equivalent to the condition:

$$|dq_v| = |dq_{ice}| \lesssim |dq_{ice,lim}| = 3 \cdot 10^{-4}, \quad (15)$$

that allows to neglect variations of atmospheric mass due to condensation of CO₂.

In what follows, temperature profiles are perturbed by the propagation of a gravity wave at each time step notwithstanding the condensation of CO₂. This is acceptable provided that the latent heat released by the phase change does not significantly affect the prescribed background temperature profiles. Given that $L_{sub} \sim 6 \cdot 10^5$ J kg⁻¹, the energy e_{lim} per kilogram of air released to the atmosphere by the formation of $|dq_{ice,lim}|$ is $e_{lim} \sim 180$ J kg⁻¹. Using the heat capacity of the CO₂/N₂ gas mixture which is close to CO₂'s ($\sim 0.7 \cdot 10^3$ J kg⁻¹), the corresponding temperature increase is $\delta T_{lim} \sim 0.25$ K. This can indeed be considered as negligible compared to typical wave perturbations. We will keep track of the quantity of ice formed during simulations and observe to which extent our trace-gas scheme is correct for the modeling of mesospheric CO₂ ice clouds.

3. Idealized simulations using Gaussian cold pockets

3.1. Gravity waves

Because gravity waves might be triggered by various sources like convection, wind shear, and topography, it is difficult to constrain the properties of the gravity waves (spatial wavelengths and time period) that might have caused the formation of the identified CO₂ clouds. This task is still not within reach of existing modeling tools

and observations of the martian atmosphere. For this reason we did not attempt to precisely reproduce each of the observed cloud events. We investigate instead two general types of clouds: the daytime ones observed by OMEGA and CRISM, and the nighttime ones inferred from SPICAM observations (Table 1). Fig. 2 shows the two temperature profiles we will be using in Section 4 with supersaturated pockets around ~ 70 – 80 km (daytime profile) and ~ 90 km (night profile). The temporal variation over the four hour run is mainly due to the propagating gravity waves. These waves perturb a profile predicted by GCM calculations and mostly controlled by thermal tides (see Fig. 5 of González-Galindo et al., 2011). Topographically-induced gravity waves were obtained from mesoscale simulations with a mountain height of 4 km and uniform background wind of 30 m s⁻¹ as described in Spiga et al. (2012) for the daytime profiles. Nighttime profiles were obtained with the same method as Spiga et al. (2012) with initial state given by a nighttime profile of González-Galindo et al. (2011).

3.2. Dust condensation nuclei

For background dust conditions we used a dust equilibrium profile obtained by initializing the run with an equal amount of dust particles in all layers of our 1D-model (with effective radius $r_{eff} = 1$ μm and variance $v_{eff} = 0.5$). We chose a log-normal distribution, since it is most representative of the asymptotic behavior of dust, compared to a gamma-modified distribution which overestimates particles smaller than ~ 100 nm (Montmessin et al., 2002). Equilibrium is achieved between vertical mixing and gravitational settling roughly after ~ 100 sols for $k_d = 100$ m² s⁻¹, and after ~ 10 sols for $k_d = 1000$ m² s⁻¹ (deposition of particles is not allowed at the surface, what mimics a supply of dust particles from the surface). Fig. 3 shows profiles of dust in equilibrium for the two values of k_d .

Typical dust profiles from average conditions in tropical regions as given by the Mars Climate Database v.5 (Millour et al., 2012) are superimposed in Fig. 3a, corresponding to observation epochs of CO₂ clouds. Our profiles with constant k_d bracket typical dust conditions during epochs of CO₂ cloud formation. The upper bound profile will be sufficient to conclude on CO₂ cloud formation and related opacities in Section 4.3. Fig. 4 displays the dust effective radius profiles for both of k_d values. For $k_d = 1000$ m² s⁻¹, at

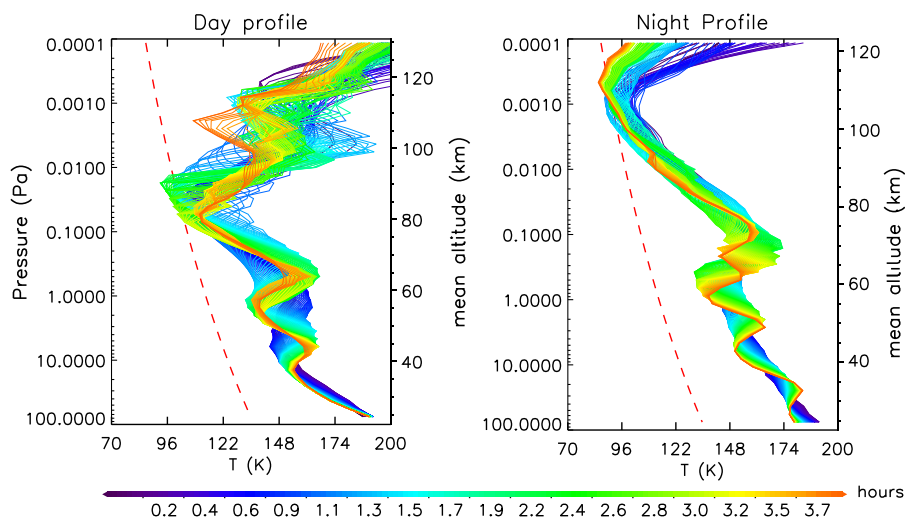


Fig. 2. Atmospheric day (left) and night (right) vertical temperature profiles perturbed by a gravity wave. Time elapsed from simulation start is given in color. Day and night large-scale temperature profiles, with absolute minima induced by thermal tides (Fig. 5 González-Galindo et al., 2011), are perturbed by topographically-induced gravity waves as explained in Spiga et al. (2012) (see text for details). The dashed line indicates the CO₂ condensation temperature. (For interpretation of the references to color in this figure legend, the reader is referred to the electronic version of this article.)

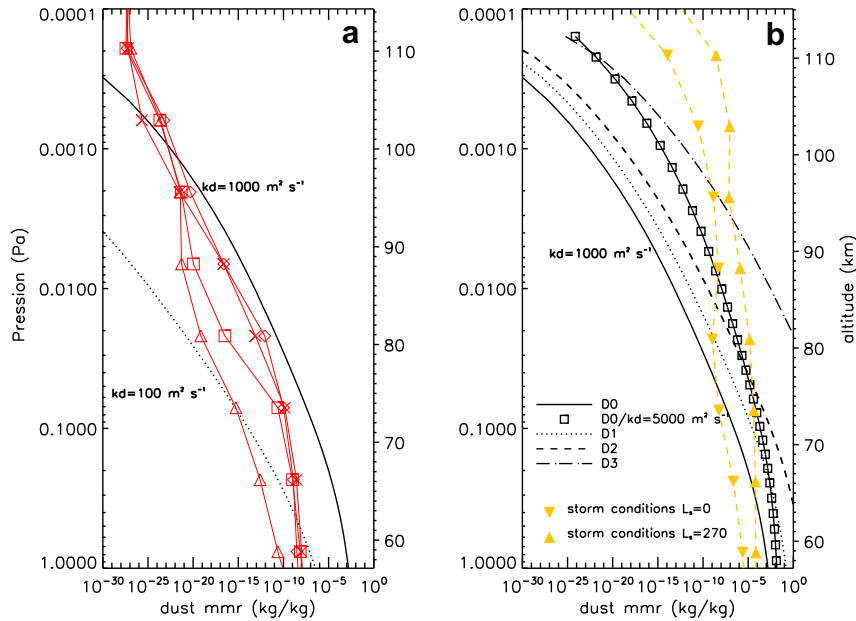


Fig. 3. (a) Vertical profiles of dust mass mixing ratios (kg/kg) obtained above 1 Pa pressure level, with eddy mixing coefficient $k_d = 100 \text{ m}^2 \text{ s}^{-1}$ (dotted line) and $1000 \text{ m}^2 \text{ s}^{-1}$ (solid line). Solid lines with symbols (in red) indicate profiles from MCD (Millour et al., 2012) representative of typical conditions during observation epochs of CO_2 ice clouds [L_s ; LT; Lat; Long]: diamonds [$0^\circ; 16 \text{ h}; 0^\circ; 0^\circ$], triangles [$45^\circ; 16 \text{ h}; 0^\circ; 0^\circ$], squares [$135^\circ; 01 \text{ h}; -15^\circ; 0^\circ$], crosses [$135^\circ; 16 \text{ h}; 0^\circ; 0^\circ$]. (b) Dust mass mixing ratio equilibrium profiles (D0–D3) obtained with $k_d = 1000 \text{ m}^2 \text{ s}^{-1}$ above 1 Pa pressure level for different initial conditions in terms of dust concentration. D0 is dust profile with $k_d = 1000 \text{ m}^2 \text{ s}^{-1}$ in figure (a). A dust profile obtained with $k_d = 5000 \text{ m}^2 \text{ s}^{-1}$ and same total dust mass as D0 is also shown. Filled upward and downward triangles correspond to dust profiles within storm conditions, shown for comparison, as extracted from (Millour et al., 2012) at $L_s = 270^\circ$ and $L_s = 0^\circ$ respectively. (For interpretation of the references to color in this figure legend, the reader is referred to the web version of this article.)

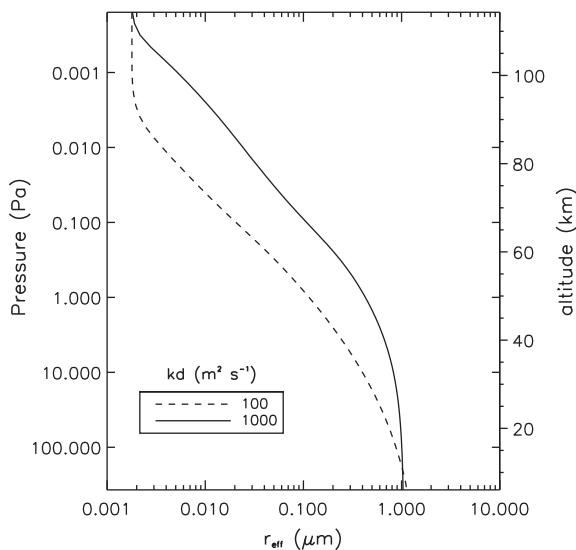


Fig. 4. Vertical profiles of dust effective radius as obtained from dust equilibrium profile for $k_d = 100 \text{ m}^2 \text{ s}^{-1}$ and $k_d = 1000 \text{ m}^2 \text{ s}^{-1}$.

altitudes ~ 70 – 80 km, dust effective radius is in the range 60 – 100 nm. At 90 km, the effective radius is around 20 nm.

3.3. First test: idealized cold pockets

We first discuss sensitivity tests with an idealized cold pocket, which is represented by a Gaussian profile. Such representation is more tunable than a simulated gravity wave (Fig. 2) obtained from mesoscale modeling (Section 4) and allows for investigating the influence of both the maximum amplitude reached by supersaturation and the time spent in supersaturated conditions.

For this purpose we use a temperature profile from the Mars Climate Database (Millour et al., 2008) from which we subtract a given perturbation δT so that $T(t, z) = T_{MCD}(t = 0, z) - \delta T(t, z)$, where:

$$\delta T(t, z) = T_M \exp \left[-(t - t_c)^2 / 2\sigma_t^2 \right] \exp \left[-(z - z_c)^2 / 2\sigma_z^2 \right], \quad (16)$$

where t is the time, z the altitude, t_c and z_c are constants related to the time and the altitude where the cold pocket reaches its peak amplitude. We separately act on both the maximum amplitude (T_M), i.e. on the maximum saturation ratio S_{max} reached, and on the time spent in supersaturated conditions (σ_t). We can also modify the vertical extent of the pocket by modifying σ_z . To simplify our discussion we fix σ_z to a constant value (3 km): all considered cold pockets have a maximum vertical extent of ~ 10 km (base of the cold pocket, where $S = 1$) and a ~ 5 km vertical extension at half-width of the Gaussian cold pocket. Fixing the average temperature T_{MCD} at $t = 0$ allows to exclusively investigate the influence of parameter σ_t in $T(t, z)$. We show in Fig. 5a two types of idealized cold pockets at different times, chosen at two different altitudes corresponding to nighttime (high altitude) and daytime (lower altitude) clouds. Note that for all simulations the daytime profile (Fig. 5a) was shifted by ~ 12 K in order to stand just above the condensation temperature, so that σ_t really represents the time spent under supersaturated conditions (as for the nighttime profile). Growth rates are derived in the model using $f_c(T_a)$ (Eq. (6)) i.e. without radiative heat transfer terms.

In Fig. 6 are shown vertical profiles (figures a, b, c, and d) and radius distributions (Figures e, f, g, and h) related to a typical CO_2 cloud simulation performed with $T_M = 6$ and $\sigma_t = 0.5$ h in Eq. (16). The cold pocket forms and reaches its maximum amplitude at $t = t_3$ (Fig. 6a) where the minimum temperature (97 K or equivalently $S = 4.5$) is reached. The effective ice radius r_{eff} is around $0.8 \mu\text{m}$ (Fig. 6b and g), and all dust particles have been activated for condensation (Fig. 6g) after a transiting phase where dust particles and crystals were still coexisting (e.g. at $t = t_2$ in

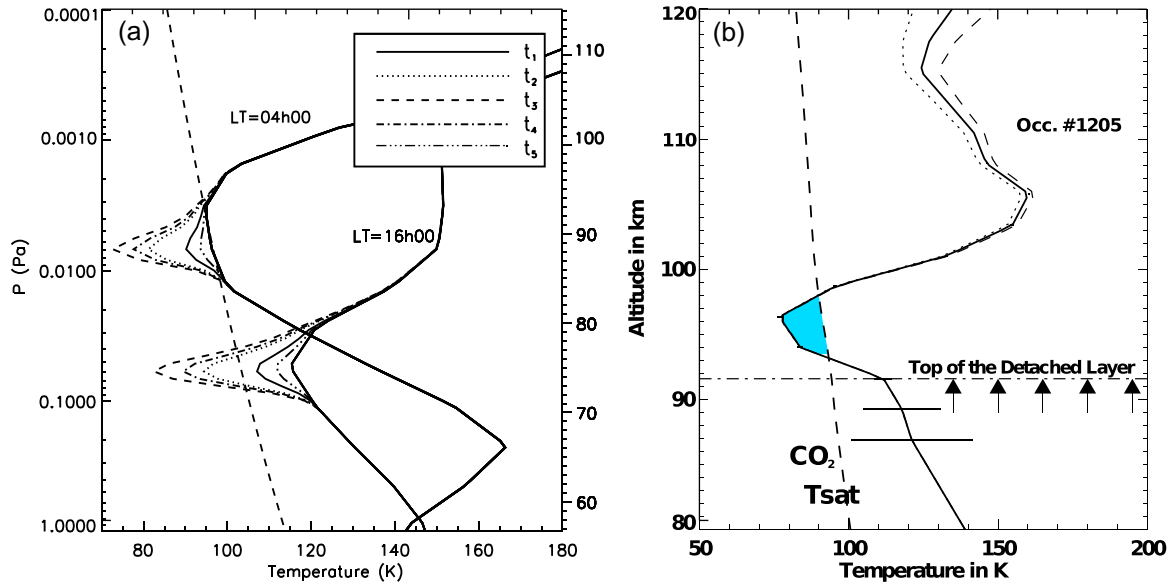


Fig. 5. (a) Examples of temperature profiles (thick lines) from the Mars Climate Database (Millour et al., 2012) modified by a Gaussian cold pocket growing and vanishing with time (thin lines correspond to different elapsed time with $t_1 \leq t_{i+1}$). Nighttime and daytime profiles are used to account for the distinct altitudes where nighttime clouds can form: here, ~ 90 km at local time 4 a.m. and ~ 70 – 80 km at local time 4 p.m. The dashed line indicates the CO_2 condensation temperature. (b) A supersaturated layer as detected by SPICAM instrument: the top of the simultaneously detected aerosol detached layer is indicated (image reused with permission, part of Fig. 4 in Montmessin et al., 2006).

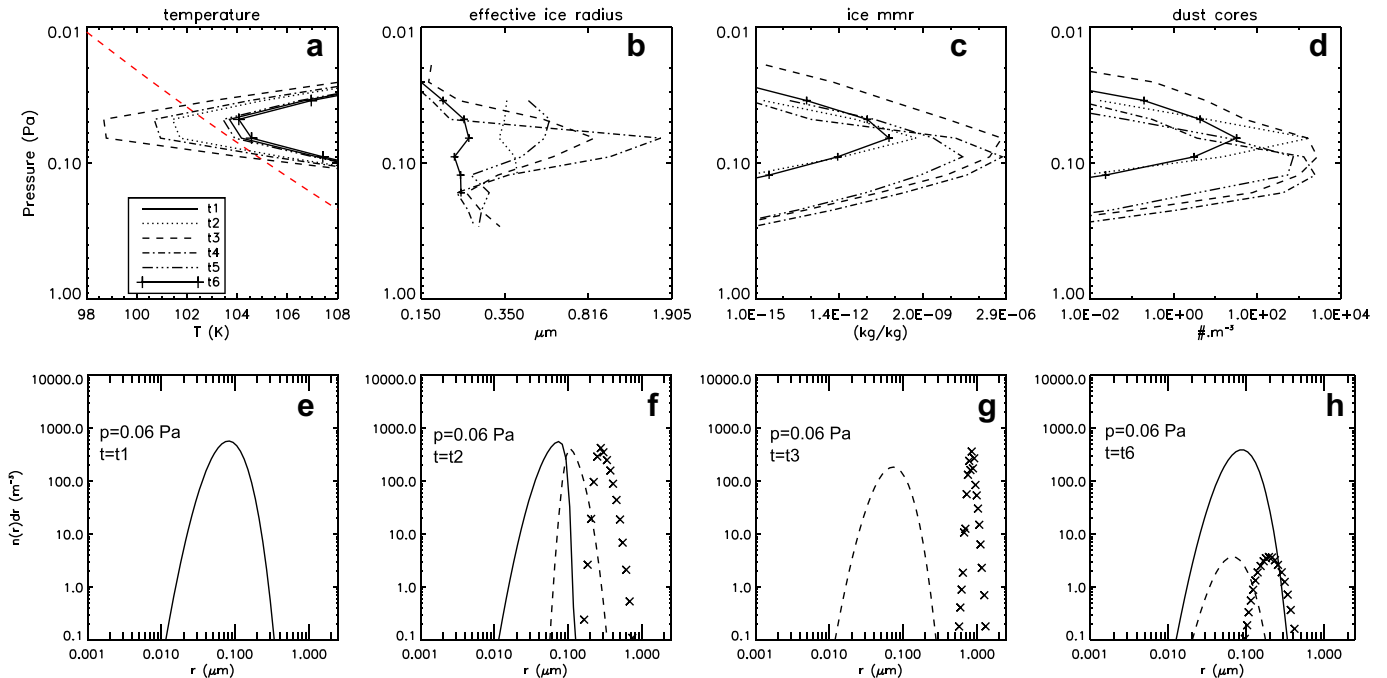


Fig. 6. Example of a cloud forming within a cold pocket (with $T_M = 6$ and $\sigma_r = 0.5$ h in Eq. (16)) created at a characteristic daytime cloud altitude (at $p = 0.05$ – 0.1 Pa, at ~ 75 km). From left to right (upper row) are plotted at different times vertical profiles of (a) the atmospheric temperatures in Kelvin, (b) the ice effective radius r_{eff} in μm , (c) the ice mass mixing ratio in kg/kg and (d) the number density of crystals (or equivalently of dust cores) in particles per m^3 . From left to right (lower row) are shown radius distributions of dust particles (solid line), dust cores (dashed line) and CO_2 ice crystals (crosses) at four distinct times related to the vertical profiles, respectively t_1 (e), t_2 (f), t_3 (g), and t_6 (h), at a pressure $p = 0.06$ Pa.

Fig. 6f). The largest growing crystals have the largest characteristic growth time, thus smaller crystals grow faster, leading to a radius distribution of crystals much narrower than the one of initial dust particles which act as CN (Fig. 6g). The crystals continue to grow as long as $T < T_{cond}$ ($S > 1$) and r_{eff} reaches $\sim 1.9 \mu m$ at $t = t_4$ (Fig. 6b). At $t = t_6$ where $T > T_{cond}$ at all altitudes, the number density of crystals has decreased by two orders of magnitude at $p = 0.06$ Pa

(Fig. 6d), and dust nuclei have been released back to unactivated dust particles (Fig. 6e). Note the extension of the cloud outside the condensation area (mainly below) due to sedimentation (Fig. 6c and d).

We summarize in Fig. 7 the different trends regarding the mean effective radii (a) and maximum effective radii (b) of CO_2 ice particles obtained for different combinations of σ_t , and T_M (or

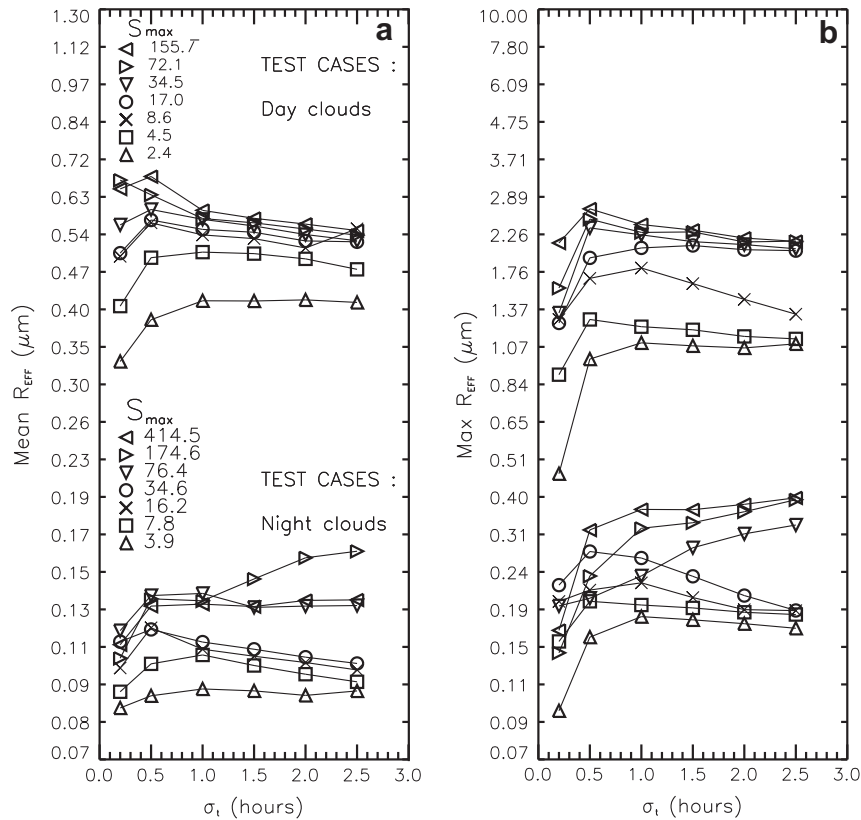


Fig. 7. Mean (a) and maximum (b) effective crystal radii in relation to σ_t (hours). Radii were determined within each simulated cloud where $0.1N_{c,max} \leq N_c \leq N_{c,max}$, with N_c the number density of crystals and $N_{c,max}$ the maximum number density reached during each simulation. Idealized Gaussian cold pockets (as in Fig. 5) are used. A single curve corresponds to a given maximum saturation ratio (S_{max}) reached for a cold pocket of increasing duration (i.e. increasing σ_t). The maximum saturation ratios reached in each case (each curve) is indicated in Figure (a) with its corresponding symbol. These values of S_{max} correspond to values of T_M ranging from 2 K to 25 K and σ_z is fixed to 3 km (see Eq. (16)). Top parts of each Figure (corresponding to larger values of radii) are related to daytime clouds, and bottom parts to nighttime clouds.

equivalently S_{max}). We use the dust equilibrium profile obtained with $k_d = 1000 \text{ m}^2 \text{ s}^{-1}$. The amplitude T_M takes values ranging from 2 K to 25 K, corresponding to saturation ratios indicated in Fig. 7. The mean and maximum effective radii (r_{eff}) plotted here are computed over the altitudes and times where the crystal number density N_c is comprised between $0.1N_{c,max}$ and $N_{c,max}$, where $N_{c,max}$ is the maximum crystal number density reached during cloud formation. The simulation previously discussed (Fig. 6) corresponds (in Fig. 7b) to the square symbols of the day clouds cases ($S_{max} = 4.5$) at $\sigma_t = 0.5 \text{ h}$ (second square of the curve, starting from left). The reason why the maximum effective radius for this simulation, reported in Fig. 7b, is different from the value reached with the vertical profiles in Fig. 6b is that the latter is reached where $N_c \leq 0.1N_{c,max}$ (outside the range characterizing the values reported in Fig. 7).

Overall, Fig. 7 allows to draw a general picture of typical effective crystal sizes obtained with these idealized simulations. Two distinct altitude ranges are associated with ranges of mean effective radius r_{eff} (Fig. 7a):

- 350–700 nm for lower altitude daytime clouds
- 80–150 nm for higher altitude nighttime clouds

The main reason for this behavior is that condensation is less efficient at higher altitudes, e.g. condensation characteristic timescales at $p \sim 0.002 \text{ Pa}$ (night profile) are ~ 10 – 100 times larger than at $p \sim 0.02 \text{ Pa}$ (day profile). The maximum supersaturation reached within the cold pocket has mainly a secondary influence; it is responsible for radius variations within each of both radius ranges identified above. The duration of the cold pocket (σ_t) is also second-

ary for the mean r_{eff} . Between the different curves (supersaturations) the largest difference in mean r_{eff} appears for the smallest σ_t . With increasing σ_t , i.e. time spent under supersaturated conditions, the difference in mean r_{eff} between different curves is generally smaller. A longer cold pocket generally allows for increased crystal sizes: at low supersaturations this results in an increased mean radius, whereas at higher supersaturations this can also result in a decreased mean radius due to sedimentation of the cloud.

The duration of a cold pocket has a stronger impact on the maximum effective radius reached within the same parts of the cloud (where $0.1N_{c,max} \leq N_c \leq N_{c,max}$). Fig. 7b displays the maximum effective radii related to the mean radii in Fig. 7a. From 0.2 h to 0.5 h the maximum effective radius can double both in the day or in the night case. The maximum radius can exceed $2 \mu\text{m}$, in agreement with the largest sizes measured by OMEGA/CRISM remote sensing observations (Montmessin et al., 2007; Määttänen et al., 2010; Vincendon et al., 2011). On the other hand the maximum radii obtained for nighttime clouds are $\geq 300 \text{ nm}$, i.e. twice the maximum observed with SPICAM spectrometer for night clouds.

4. Reproducing CO_2 mesospheric clouds within realistic wave-induced cold pockets

We now turn to the nighttime and daytime temperature profiles (Fig. 2) obtained from mesoscale modeling where gravity wave propagation is reproduced in a four hour run. Using mesoscale simulations allows to account for temporal variations of gravity waves, putatively giving rise to cold pockets, propitious to CO_2

cloud formation. Large-scale temperature profiles used to initiate the mesoscale profiles come from the LMD-GCM (Forget et al., 1999) extended up to the exosphere (González-Galindo et al., 2009). Mesospheric temperatures obtained with this GCM yield values, which can be warmer than temperature measurements through stellar occultations performed with SPICAM (Forget et al., 2009) by up to 15 K, at altitudes higher than ~ 70 km. Thus, the entire profile is shifted in temperature by subtracting a constant value of $\Delta T_{\text{shift}} < 15$ K in order to investigate a broad range of mesospheric supersaturations, where CO_2 clouds could form. Shifting the temperature profiles by ΔT_{shift} means shifting the large-scale temperature profile. The gravity wave amplitude remains unchanged. Forcing the average temperature profile to be colder by ΔT_{shift} than what the GCM predicts, in the lower mesosphere and in the troposphere, has no influence on our conclusions in the highest layers of the mesosphere (≥ 70 km). Indeed, the simulated clouds evaporate before reaching these lower altitudes.

We are interested in the formation of CO_2 clouds induced by gravity wave activity, which causes the formation of a transient cold pocket in the mesosphere. Fig. 8 shows two typical cold pockets with their corresponding saturation ratios (S). In this example S reaches values up to several tens at maximum, around 70–80 km for the day profile where $\Delta T_{\text{shift}} = 5$ K (Fig. 8a). It corresponds to temperature differences up to 10 K with the condensation temperature of CO_2 in agreement with the Pathfinder measurements (Schofield et al., 1997) at such altitudes. S reaches several hundreds and even $S \sim 1000$ at the highest altitudes for the night profile with $\Delta T_{\text{shift}} = 10$ K (Fig. 8b), in agreement with SPICAM measurements (Montmessin et al., 2006, 2011; Forget et al., 2009).

At the end of this section, Table 2 summarizes the main simulation results discussed in the text.

4.1. CO_2 mesospheric clouds under typical dust conditions

4.1.1. Daytime clouds with the CLASSIC model

We discuss the results obtained with the reference CLASSIC model where growth rates are derived using the iterative

resolution of f_c given by Eq. (6). Temperatures are given by the set of day profiles plotted in Fig. 2 (left). When $\Delta T_{\text{shift}} = 0$ K (not shown), saturation ratios are always below 9.5 (peak reached at 2.4 h). When $\Delta T_{\text{shift}} = 5$ K, saturation ratios increase up to 67 in the cold pocket (peak reached at 2.4 h). We use the typical dust profile with $k_d = 1000 \text{ m s}^{-1}$. Cloud opacity, τ , is vertically integrated on the atmospheric column and is derived as follows:

$$\tau = \int_z \left[\int_0^\infty N_c(z, r) \times \pi r^2 \times Q_{\text{ext}}(r) dr \right] dz, \quad (17)$$

where z is the altitude, r the crystal radius, $N_c(z, r)$ the crystal number density at altitude $z \pm dz$ of crystals of radius $r \pm dr$, and $Q_{\text{ext}}(r)$ the extinction efficiency for a crystal of radius r (assumed as being pure CO_2 ice) and computed according to Mie theory with optical constants of CO_2 ice taken from Hansen (1997, 2005).

Fig. 9 shows the crystal effective radius (top) and crystal number density (bottom) as a function of pressure and elapsed time. The cloud opacity at 1 μm and 500 nm is also shown. Interestingly, for $\Delta T_{\text{shift}} = 5$ K, r_{eff} reaches comparable values to the ones derived from OMEGA and CRISM data (i.e. around $\sim 1 \mu\text{m}$). Note that for $\Delta T_{\text{shift}} = 0$ K (not shown), $r_{\text{eff}} \sim 300$ nm at maximum, which is close to the lowest value suggested by CRISM observations (~ 500 nm). However, the maximum opacity is four orders of magnitude smaller than average opacities measured by OMEGA and CRISM. The maximum opacity τ_{max} is obtained when both r_{eff} and N_c (around $t = 3.3$ h in Fig. 9), with values of 1.3 μm , and 10^3 m^{-3} respectively. Opacity τ is maximum just before the cold pocket vanishes since, as long as $S > 1$, crystals continue to grow (except for crystals < 100 nm, for which curvature effect is responsible for evaporation for $S > 1$). Then τ decreases by a factor of 10 after ~ 20 min, and N_c decreases from 10^3 m^{-3} to $\sim 10 \text{ m}^{-3}$.

The vertical extent of the cloud is mainly controlled by the vertical extent of the cold pocket. The upward extension of the cloud (compared to the cold pocket) is caused by the vertical mixing. The largest crystal number densities are found in the supersaturated area, or below the supersaturated area owing to the displacement of the cold pocket (e.g. at $t = 2.3$ just above $p = 0.1$ Pa) or due to sedimentation (e.g. the highest crystal number densities at $t > 3$ h).

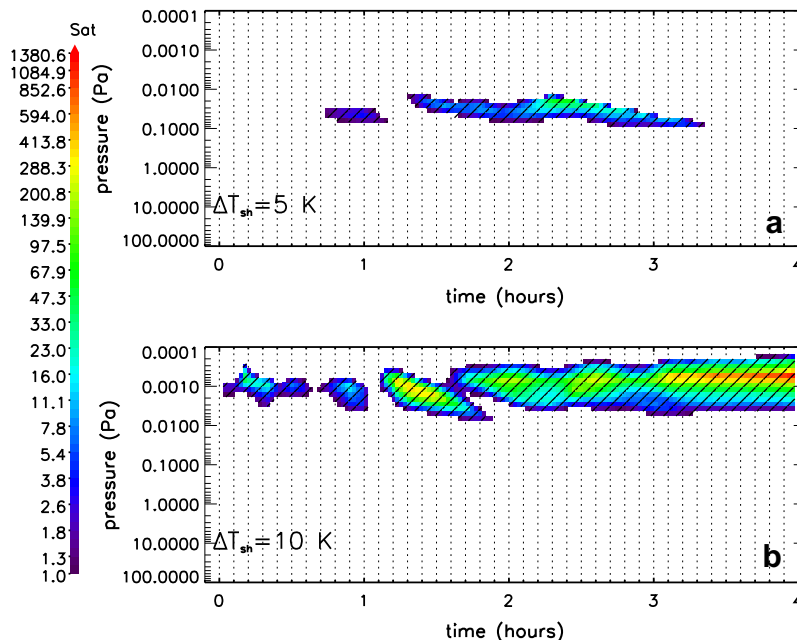


Fig. 8. Saturation ratio S (colors) versus elapsed time (hours) plotted whenever $S \geq 1$, for (a) day temperature profiles with $\Delta T_{\text{shift}} = 5$ K, and (b) for night temperature profiles with $\Delta T_{\text{shift}} = 10$ K. See beginning of Section 4 for details. Vertical axis is atmospheric pressure (Pa). The shaded area corresponds to altitudes where $S > 1$, and will be used as an indicator of supersaturated area in the next plots. (For interpretation of the references to color in this figure legend, the reader is referred to the web version of this article.)

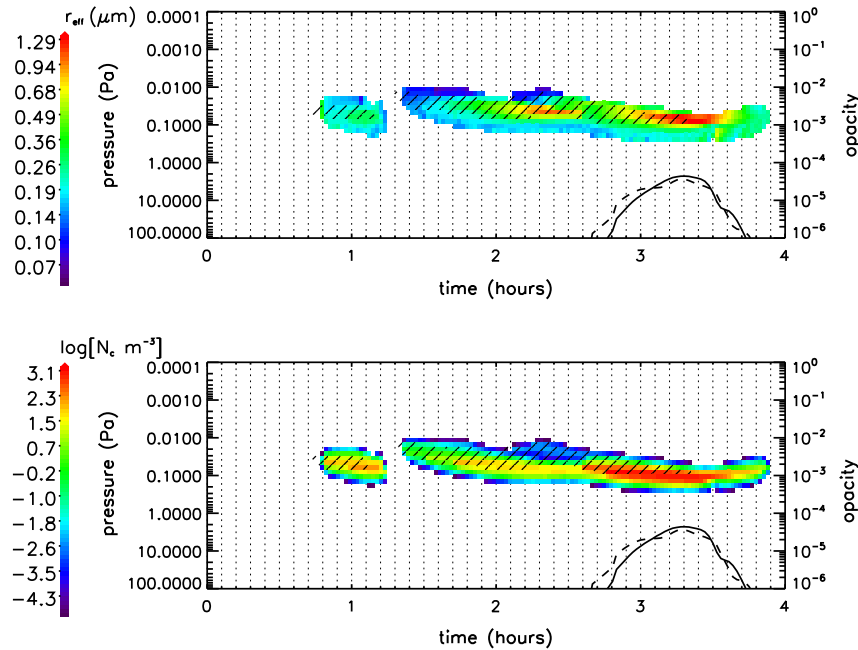


Fig. 9. Crystal effective radius (μm , top) and Crystal number density (in m^{-3} log-scale, bottom) versus elapsed time (in hours) for a daytime clouds with the CLASSIC (non-linearized) model, plotted every 100 s. $\Delta T_{\text{shift}} = 5$ K. Vertical axis for the color-shaded plot is pressure (left). In addition the total vertical opacity is plotted (black lines), with the vertical axis on the right, for wavelengths $\lambda = 0.5$ m (dashed) and $\lambda = 1$ m (solid) related to OMEGA (Montmessin et al., 2007; Määttä et al., 2010) and CRISM observations respectively (Vincendon et al., 2011). The shaded area shows where the atmosphere is supersaturated ($S > 1$) with respect to CO_2 ice, and corresponds to saturation ratios plotted in Fig. 8a. (For interpretation of the references to color in this figure legend, the reader is referred to the web version of this article.)

However, crystals do not persist a long time in a sub-saturated air: the cloud disappears quickly after the cold pocket has vanished (~ 20 min).

Finally, variations of the vapor mixing ratio dq_v are far below the limit fixed in Section 2.3 for the trace gas approach: $dq_{\text{ice,max}} \sim 10^{-6}$ for $\Delta T_{\text{shift}} = 5$ K, and $dq_{\text{ice,max}} \sim 10^{-8}$ for $\Delta T_{\text{shift}} = 0$ K.

4.1.2. Nighttime clouds with the CLASSIC model

We show that we reproduce from our typical dust scenario an effective size for crystals close to what has been derived by Montmessin et al. (2006) for nighttime clouds. The temperature is given by the set of nighttime profiles plotted in Fig. 2 (right) with $\Delta T_{\text{shift}} = 10$ K. Results for the CLASSIC model are presented in Fig. 10 with effective radius of crystals (top) along with the corresponding crystal number densities (bottom). We investigate the evolution of very low concentrations of crystals created in the cold pocket which corresponds to the shaded area in Fig. 10. At the highest altitudes, saturation ratios reach several hundreds, up to $S \sim 1000$. This is of the order of magnitude measured in the highest layers of the martian mesosphere (Forget et al., 2009; Montmessin et al., 2011). The crystal effective radius r_{eff} reaches ~ 75 nm at 0.01 Pa (~ 90 km), in accordance with the lowest average sizes observed by Montmessin et al. (2006). The ice mass change $dq_{\text{ice,max}} \ll 10^{-4}$ so that our trace-gas approximation is valid. The main part of the cloud forms at altitudes where S is about a few hundreds (~ 300 at 1.3 h), after which S decreases with time, before increasing again later on at higher altitudes (Fig. 8b). N_c reaches $5 \cdot 10^{-5} \text{ m}^{-3}$ at its maximum. The altitude range where the cloud forms (90–100 km) is comparable to the altitudes reported by Montmessin et al. (2006); yet opacities at 200 nm are far below the opacities derived by Montmessin et al. (2006).

Around 1.9 h (Fig. 10) the cloud is still present around $p \sim 0.01$ Pa while the cold pocket has just vanished at this pressure level. To emphasize this feature we focus on some specific vertical profiles

around 1.9 h, as shown in Fig. 11a. We found that the main cloud is created by a secondary supersaturated pocket below the main one (Fig. 11a). This lower cold pocket (where saturation ratios are much lower than above) triggers crystal growth and vanishes, due to the temporal pattern of the wave, letting the layer evaporate underneath the biggest cold pocket, which remains above. The cloud that formed vanishes quickly after (~ 10 min). Thus we show that a pattern similar to the one observed by Montmessin et al. (2006) (an altitude shift between the supersaturated area and the detached aerosol layer) can possibly be explained by the gravity wave temporal behavior.

4.1.3. Effect of radiative heat transfer

Here we explain how the inclusion of radiative heat transfer in the crystal energy budget of the CLASSIC model modifies the results for both daytime and nighttime clouds. We use $f_{c,\text{rad}}(T_a)$ (Eq. (13)) instead of $f_c(T_a)$, to solve for T_a and to derive the crystal growth rate. We investigate the effect of radiative heat transfer on the cases described above, which allowed to obtain effective radii in accordance with observations. The radiative cooling term enhances by roughly 7% (from ~ 1.3 to $\sim 1.4 \mu\text{m}$) the effective radius for the daytime cloud in the case where $\Delta T_{\text{shift}} = 5$ K. Thus, heat released by condensation is only marginally lost by radiative cooling, and mainly by heat conduction. Adding the solar and IR heating reduces the net amount of vapor condensing and decreases the maximum effective crystal size to $\sim 0.60 \mu\text{m}$ as shown in Fig. 13 (bottom). This is still in the range of effective sizes derived from measurements (especially above the lower limit measured by Vincendon et al. (2011)). To compensate for the heating and to obtain sizes $> 1 \mu\text{m}$, we need a shift $\Delta T_{\text{shift}} = 10$ K in temperature. This ΔT_{shift} value might be unrealistically high: it is equivalent to saturation ratios reaching ~ 600 , which is closer to the supersaturations observed in upper layers of the night mesosphere (~ 100 km and above) than around 70–80 km. The inclusion of radiative heat transfer terms for nighttime clouds (solar heating P_{sol} is set to 0),

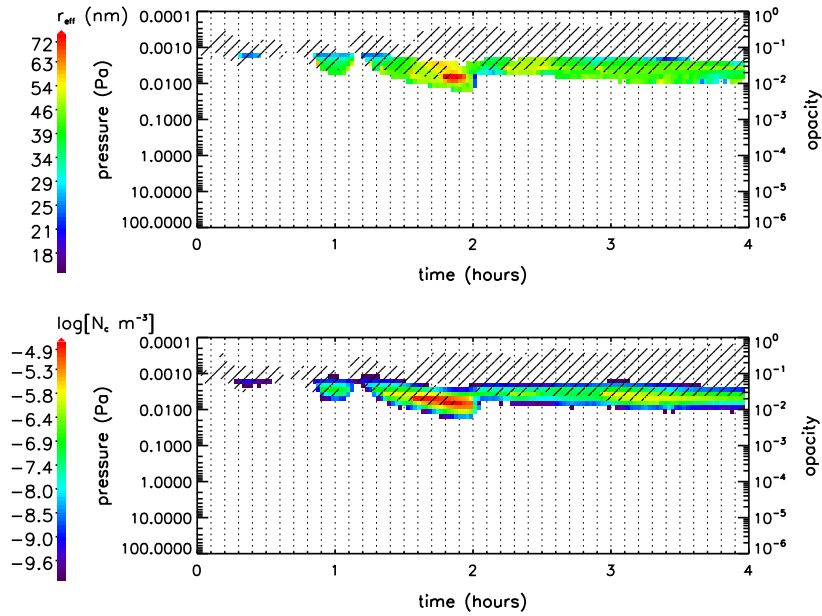


Fig. 10. Crystal effective radius (nm, top) and Crystal number density (in m^{-3} log-scale, bottom) versus elapsed time (in hours) for a nighttime cloud with the CLASSIC (non-linearized) model, plotted every 100 s. $\Delta T_{\text{shift}} = 10$ K. Figure axes are as above (Fig. 9) except that opacity (right axis) is derived at $\lambda = 200$ nm. Opacity is $\ll 10^{-6}$. Shaded area indicates supersaturated area ($S > 1$), and corresponds to saturation ratios plotted in Fig. 8b. (For interpretation of the references to color in this figure legend, the reader is referred to the webversion of this article.)

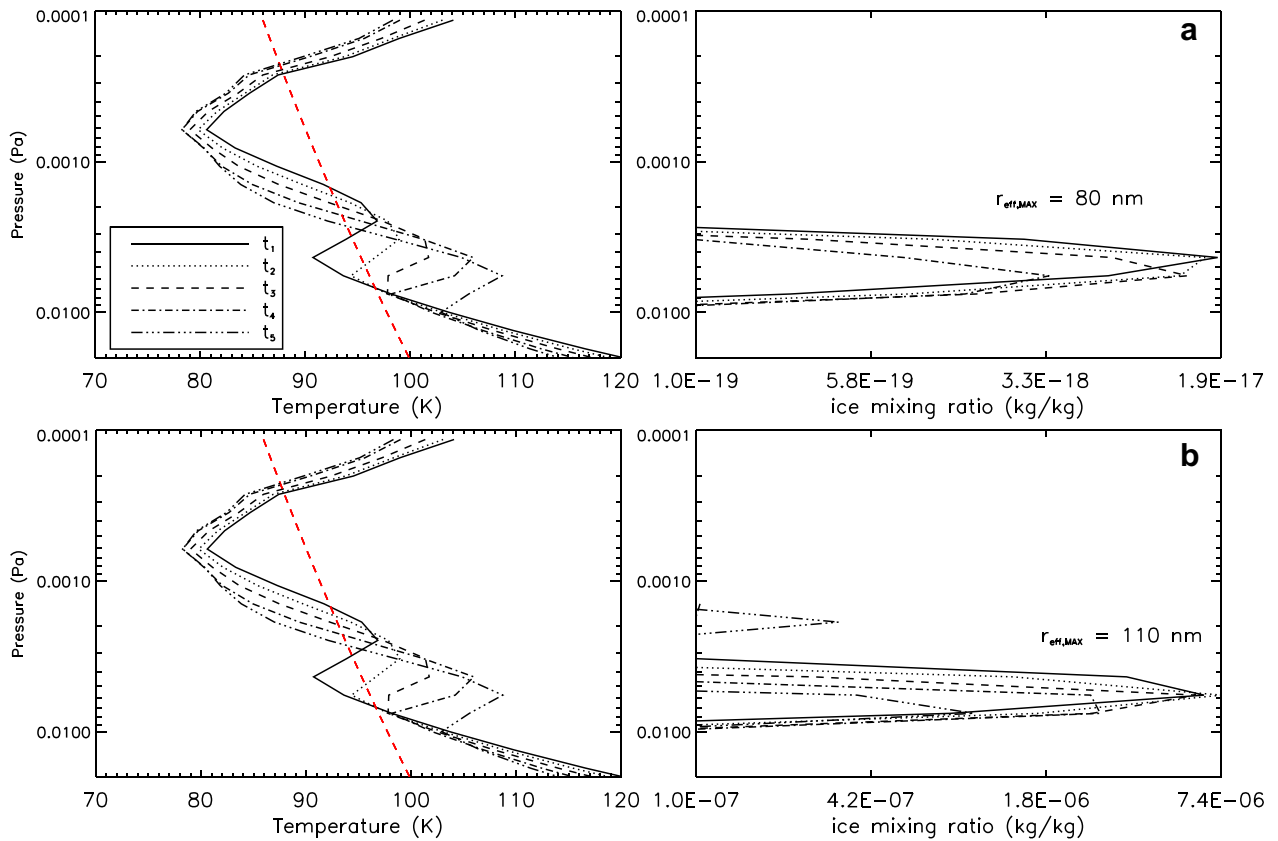


Fig. 11. (a) Selection of specific vertical profiles of atmospheric temperature (left) and ice mass mixing ratio (right), from cloud simulation shown in Fig. 10. Profiles are shown starting from 1.9 h (elapsed time), and plotted every 200 s, to emphasize the shift in altitude appearing between the cold pocket (~ 0.001 Pa), and the cloud below. (Solid line, dashed line, dot-dashed line and triple-dot-dashed line correspond, in this order, to increasing time.) The red dashed line indicates the CO_2 condensation temperature. (b) Same as (a) but related to cloud simulation shown in Fig. 18.

has no consequences on effective sizes. Indeed, the maximum crystal radius $r_{\text{max}} (\neq r_{\text{eff}})$ registered in the simulation reduces in size by

40 nm (from 150 to 110 nm) owing to the heating term P_{atm} , but the largest crystal radii have the lowest concentrations, and overall

the effective radius r_{eff} of crystals does not vary. The smaller crystal sizes at these altitudes are less sensitive to IR flux absorption (smaller cross-section). Furthermore, the radiative cooling term is smaller than the heat conduction term which dominates the cooling process during condensation.

Solar heating $P_{\text{sol}}(r)$ is derived assuming that the solar flux comes from above the crystal. This would be true at zero solar zenith angle (SZA). However, most OMEGA and CRISM CO₂ clouds were observed in the morning (8 am) or in the afternoon (4–5 pm). At these local times the solar flux could be scattered by aerosols and gases. Hence $P_{\text{sol}}(r)$ can be considered as an upper estimate of the solar input. $P_{\text{atm}}(r)$ is an upper estimate as well because we assume that half of crystal surface ($2\pi r^2$) absorbs the same IR flux, taken from the MCD as the IR flux to space. Crystals in the center of the clouds will be differently, and possibly less, influenced by both the solar and IR flux, due to screening of the crystals at the edges of the layer (which scatter/absorb the incoming fluxes depending on wavelength).

Overall, for a given radius r , including $P_{\text{sol}}(r)$ and $P_{\text{atm}}(r)$ to all crystals of radius r in the cloud should lead to an overestimation of the real influence of both heating terms. This would explain why we need to have a large temperature shift ($\Delta T_{\text{shift}} = 10$ K), and $S \sim 600$ to obtain $r_{\text{eff}} \geq 1 \mu\text{m}$ in the cloud with the radiative heat transfer added (instead of $\Delta T_{\text{shift}} = 5$ K and $S \sim 60$ without radiative transfer). However, a full radiative transfer code would be needed to assess the respective contributions of the heating terms on cloud crystals. The radiative cooling term $P_{\text{cool}}(r, T_a)$ is a radiative term, which is not related to particular assumptions regarding the radiative bath in which the crystal forms, and is found to have a minor impact in both day and night simulations.

4.2. Benefits from using the non-linearized model (CLASSIC): comparison with a linearized model (LIN)

We investigate the highly supersaturated mesospheric environment of Mars where appropriate growth rates are key to reach robust conclusions. The CLASSIC model is theoretically adapted to high supersaturations of CO₂ (Listowski et al., 2013). The growth rate models dealing with trace gas condensation, like H₂O on Earth or Mars, rely on the linearization of the saturation vapor pressure with respect to the temperature difference between the

crystal surface and the environment (linearization of the exponential term in Eq. (5)). These linearized growth rate models have been broadly used within 1D cloud models dealing with H₂O condensation on Mars (e.g. Michelangeli et al., 1993; Montmessin et al., 2002; Montmessin et al., 2004) and for CO₂ condensation on Mars as well (Colaprete and Toon, 2003; Colaprete et al., 2008). A linearized model (hereafter, LIN model) is convenient because it gives an explicit analytical formula for the growth rate of crystals, which can then be written (see e.g. Montmessin et al., 2002):

$$\frac{dr}{dt} = \frac{1}{a} \frac{S - S_{\text{eq}}}{R_d + R_h \times S_{\text{eq}}}, \quad (18)$$

where R_d , R_h are resistances to growth due to diffusion and heat conduction respectively, $R_d = \rho_{\text{ice}}RT / (M_v D p_{\text{sat}}(T))$ and $R_h = \rho_{\text{ice}} M_v L_{\text{sub}}^2 / (KRT^2)$. However, the LIN model deviates from the accurate solution when investigating high supersaturations of CO₂, due to large temperature differences between the crystal surface and the environment (Listowski et al., 2013).

Simulation results from the non-linearized model (CLASSIC) and linearized model (LIN) are compared for the daytime cloud (in Fig. 12a and b) and for the nighttime cloud (in Fig. 12c and d), corresponding respectively to simulation shown in Figs. 9 and 10. The use of the non-linearized model adapted to high supersaturation results in a cloud with smaller radii, lower opacities, and shorter lifetime than with the LIN model. While r_{eff} reaches $\sim 3 \mu\text{m}$ with the LIN model for $\Delta T_{\text{shift}} = 5$ K (Fig. 12b), the CLASSIC model gives $\sim 1 \mu\text{m}$ (Fig. 12a). For $\Delta T_{\text{shift}} = 0$ K (not shown), in the same way, the maximum effective radius is ~ 300 nm for the CLASSIC model and ~ 600 nm for the LIN model. The LIN model causes an increase in opacity by a factor ~ 10 in the $\Delta T_{\text{shift}} = 5$ K case (a bit less for $\Delta T_{\text{shift}} = 0$ K). The LIN model causes crystals to grow faster when $S > 1$, and when the cold pocket has vanished the crystals evaporate slower. The crystal population persists in the subsaturated air for a longer time (Fig. 12b) than with the CLASSIC model (Fig. 12a). Opacity decreases equally fast for both models, however concentrations of crystals with $r_{\text{eff}} \sim 100$ nm remain relatively large ($\sim 10^{13} \text{ m}^{-3}$) for ~ 30 min, longer in the LIN model as compared to the CLASSIC model.

We focus around the time 1.2 h (Fig. 12a): a small cold pocket, that had appeared and reached a $S \sim 3.5$ at its maximum (see Fig. 8a), is now disappearing, and so is the cloud with the CLASSIC

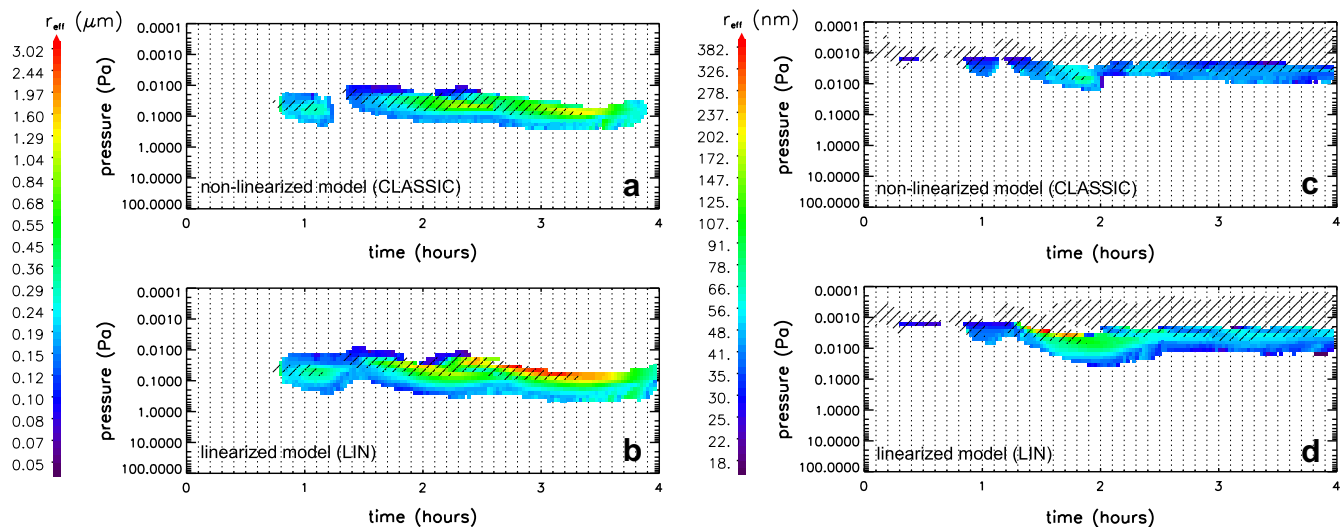


Fig. 12. Crystal effective radius (colors, left: μm right: nm) versus elapsed time (in hours). Figure axes are as in Fig. 9, except that opacity is not shown. Comparison of cloud simulations performed (a and c) with our non-linearized CLASSIC growth model (Listowski et al., 2013) and (b and d) with a linearized trace-gas model (see text for details). Left panels (a and b) are related to a daytime cloud with (a) corresponding to the cloud in Fig. 9. Right panels (c and d) are related to a nighttime cloud with (c) corresponding to the cloud in Fig. 10. Shaded area indicates supersaturated area ($S > 1$), and corresponds to saturation ratios plotted in Fig. 8a and b. (For interpretation of the references to color in this figure legend, the reader is referred to the web version of this article.)

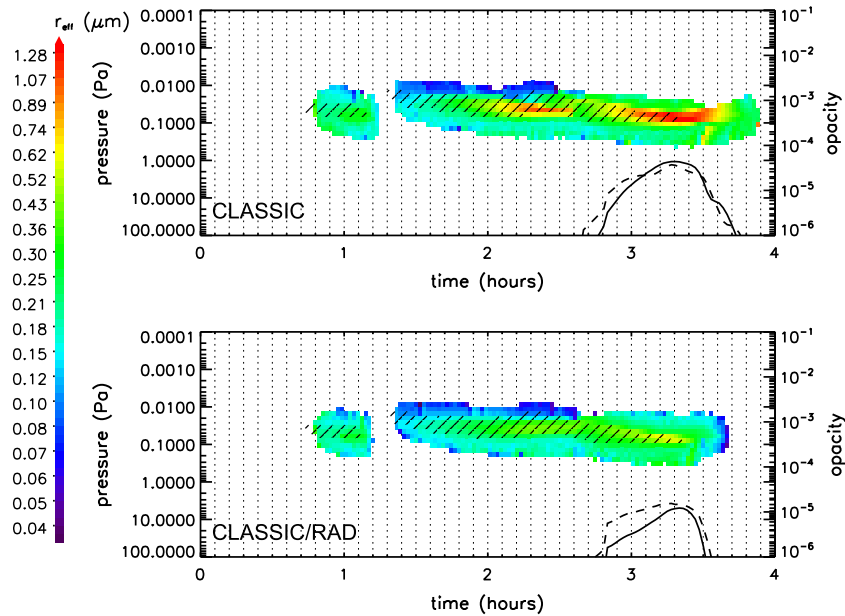


Fig. 13. Crystal effective radius (μm , colors) versus time (h) for daytime clouds for both CLASSIC model (top) and CLASSIC model with radiative heat/cooling terms in crystal growth rate (bottom). $\Delta T_{\text{shift}} = 5$ K. Figure axes are as in Fig. 9. Shaded area indicates supersaturated regions ($S > 1$), and corresponds to saturation ratios plotted in Fig. 8a. (For interpretation of the references to color in this figure legend, the reader is referred to the web version of this article.)

model. Conversely, with the LIN model (Fig. 12b), opacity is decreasing but a population of crystals with $r_{\text{eff}} \sim 100$ nm remains with a concentration of $\sim 10 \text{ m}^{-3}$ (not shown), until another cold pocket appears, reactivating condensation. The LIN model, which is theoretically wrong for high supersaturations (Listowski et al., 2013), is overestimating the cloud lifetime. The CLASSIC growth model simulates a cloud whose formation and lifetime is more directly linked to the appearances/disappearances of the cold pocket.

For the nighttime clouds, a larger vertical extent of the cloud is obtained with the LIN model (12d) compared to the CLASSIC model (12c), owing to the sedimentation of larger crystal radii. Effective radius r_{eff} is ~ 150 nm (at maximum opacity), i.e. twice as large as with the CLASSIC model. Values up to 300–400 nm are even reached with the LIN model around 1.5 h (12d), while the CLASSIC model yields value of 75 nm maximum (12c).

The LIN model yields effective radii up to 2–3 times larger than the CLASSIC model, and opacities ~ 10 times larger than the CLASSIC model in our simulated clouds, with longer lifetime and greater vertical extent of the clouds.

4.3. Reaching the observed CO_2 ice clouds opacities in the mesosphere

4.3.1. Sources for condensation nuclei

From the previous simulations, we can conclude that dust as given by the equilibrium profile with $k_d = 1000 \text{ m}^2 \text{ s}^{-1}$ is not sufficient to reach opacities observed by the different instruments (Table 1). Two approaches are considered to increase the number of CN: (1) increase the dust loading conditions of Fig. 3a to those typical of the dust storm season (Fig. 3b), or (2) add another source of particles which can serve as CN.

First, we introduce new equilibrium profiles with increased amounts of dust (Fig. 3b). As indicated on the plot, we call D1, D2, D3 the three new profiles, and D0 corresponds to the one used in the previous section. They were obtained in the same way as D0, but with an increased initial dust mass in each radius bin before letting the dust sediment and reach an equilibrium. Fig. 3b also shows two profiles of dust mass mixing ratio typical of dust storm conditions at $L_s = 270^\circ$ (filled upward triangles) and

$L_s = 0^\circ$ (filled downward triangles). Dust mass mixing ratios clearly exceed the values of our profiles with $k_d = 1000 \text{ m}^2 \text{ s}^{-1}$, above ~ 70 km. A dust profile obtained with $k_d = 5000 \text{ m}^2 \text{ s}^{-1}$ is also indicated (hereafter designated by D0/5000). It was obtained with the same initial amount of dust than D0, the only difference being the larger value of k_d . This high value of k_d can also be considered as relevant for the highest layers of the mesosphere (Izakov, 2007). Typically, an increased vertical mixing (higher k_d value) allows for the presence of larger particles at a given altitude (increasing also the dust mass), whereas D1–D3 profiles (obtained with the same $k_d = 1000 \text{ m}^2 \text{ s}^{-1}$) only increase the number of particles at a given altitude, compared to D0. MCD dust storm-scenario profiles (Millour et al., 2012) are overplotted for comparison. Although the shapes of dust profiles given in Fig. 3b are different from the MCD ones, we can say that D1 and D3 curves work as approximate lower and upper limits respectively for the MCD dust storm profile at $L_s = 270^\circ$, between 70 and 90 km. The profile with $k_d = 5000 \text{ m}^2 \text{ s}^{-1}$ better reproduces qualitatively the dust storm profile at $L_s = 270^\circ$ between 70 and 80 km.

Another approach consists in adding a constant production rate of particles at a given altitude. This new source stands for the production of particles from the ablation of meteoroids. As it will be further discussed in Section 5, particles coming from interplanetary space are believed to constantly fall into the martian atmosphere (as it is known to happen on Earth) although no direct observations of meteoritic particles have been made so far. This condensation nuclei were already suggested for PMC formation on Earth by e.g. Turco et al. (1981) and Rapp and Thomas (2006), and meteoritic material was recently observed embedded in PMC's crystals (Hervig et al., 2012). Meteoroids are ablated when falling into planetary atmospheres. Adolfsson et al. (1996) have shown that the altitude range where ablation can theoretically occur on Mars lies in the mesosphere, between ~ 50 km and ~ 90 km, thus in the altitude range where both day and night CO_2 clouds can form. The recondensation of vaporized meteoritic material provides new condensation nuclei, known as 'meteoric smoke particles' (Hunten et al., 1980). This denomination also includes their coagulation products. Typical sizes of meteoric smoke

particles in the high Earth mesosphere would range, in order of magnitude, between ~ 1 nm and ~ 10 nm (Hunten et al., 1980; Bardeen et al., 2008).

Production rate was chosen in accordance with meteoritic supply of recondensed material (per year) as estimated by Flynn (1992): $\mathcal{F} = 2 \cdot 10^6$ kg per year. With this value we can derive an order of magnitude estimate for average production rates. Then by assuming that the flux is homogeneous (with R_M the radius of Mars), the flux per surface area F_M is:

$$F_M = \frac{\mathcal{F}}{4\pi R_M^2} = 2.4 \cdot 10^{-16} \text{ kg s}^{-1} \text{ m}^{-2}$$

Considering spherical particles, the production rate $F_p(r)$ of particles of radius r (assuming single mode) is: $F_p(r) = F_M / (\frac{4}{3}\pi r^3 \rho)$. With $\rho = 2500 \text{ kg m}^{-3}$ (equal to the average martian dust density) we get:

$$F_p(1 \text{ nm}) = 2 \cdot 10^8 \text{ s}^{-1} \text{ m}^{-2},$$

and

$$F_p(10 \text{ nm}) = 2 \cdot 10^5 \text{ s}^{-1} \text{ m}^{-2}.$$

We discuss in Section 5 the density for such ablated particles. Since recondensed material coagulates after ablation (Hunten et al., 1980; Bardeen et al., 2008) we can assume that, in our simple approach, 10 nm particles come from coagulation of 1 nm as an alternative to direct formation.

4.3.2. Opacities of daytime clouds

Increased amounts of dust, close to atmospheric loadings caused by dust storms, are first investigated by setting up simulations using a range of dust profiles. In the following we derive growth rates by resolving $f_c(T_a) = 0$, i.e. without radiative terms. By using the D1 profile instead of D0, and keeping $\Delta T_{\text{shift}} = 5$ K, the simulated opacities reach $\sim 10^{-3}$, i.e. 2 orders of magnitude higher than when using D0, while $r_{\text{eff}} \sim 1.4 \mu\text{m}$ remains comparable (not shown).

In terms of opacities, this is still two orders of magnitude below the average value measured with OMEGA and CRISM. With the $D0/k_d = 5000 \text{ m}^2 \text{ s}^{-1}$ profile (hereafter D0/5000), opacities also reach $\sim 10^{-3}$ (not shown), suggesting that a more efficient vertical

mixing alone is not enough to bring typical dust content to such amounts where it could lead to observed cloud opacities. Simulations starting from a dust content D2 but with $\Delta T_{\text{shift}} = 1$ K, yield opacities of $5 \cdot 10^{-2}$ with r_{eff} reaching ~ 500 nm (Fig. 14). This is close to the order of magnitude (~ 0.1) measured by both OMEGA and CRISM instruments and around the lower values of observed crystal sizes by day. The profile D2, with $\Delta T_{\text{shift}} = 2$ K, yields opacities of 0.1 (not shown) with r_{eff} reaching ~ 800 nm (not shown). However, in terms of vapor depletion $dq_{\text{ice,max}} = 5|dq_{\text{ice,lim}}|$ ($dm_a/ma \sim 5\%$). The trace-gas approximation reaches its limit regarding dust scenarios that would allow to exactly match the observed opacities.

The production rates F_p are now added over the D0 dust profile to account for meteoritic material falling (abating) in the martian mesosphere. Fig. 15a shows the behavior of monodispersed population of particles of 10 nm particles falling into the supersaturated area ($\Delta T_{\text{shift}} = 1$ K). They are injected around 90 km altitude, in the altitude range where ablation can occur. In the case of 10 nm particles, gravitational settling is more pronounced compared to upward vertical mixing. In the case of 1 nm particles (not shown), propagation occur also upward due vertical mixing and less efficient sedimentation. Note that when adding to the D0 profile a production rate $F_p(1 \text{ nm})$ of 1 nm particles (not shown), they are not activated for condensation due to low supersaturations ($S \leq 70$) compared to the critical saturation ratio for this size (see Fig. 1). Increasing the temperature shift to $\Delta T_{\text{shift}} = 10$ K ($S \leq 600$) allows to activate all the 1 nm particles, which however cannot grow to significant sizes so that opacity remains lower than 10^{-4} . The gravity wave does not sustain the highest saturation ratios long enough for these particles to pursue their growth.

When adding the production rate $F_p(10 \text{ nm})$ and $\Delta T_{\text{shift}} = 1$ K (Fig. 15a) the dust particle number density decreases where the cold pocket forms (shaded area on the plot) due to their activation as dust cores. The 10 nm particles are activated for growth as soon as S reaches ~ 3 (Fig. 1), and S reaches ~ 15 at maximum. The maximum effective radius is $0.8 \mu\text{m}$ (Fig. 16). Note that until 2.2 h, the ice crystals effective size is $\sim 0.2 \mu\text{m}$. Then it rapidly decreases because of the activation and growth of the abundant 10 nm particles, due to saturation ratio reaching ~ 3 . Then the radii increase, because of

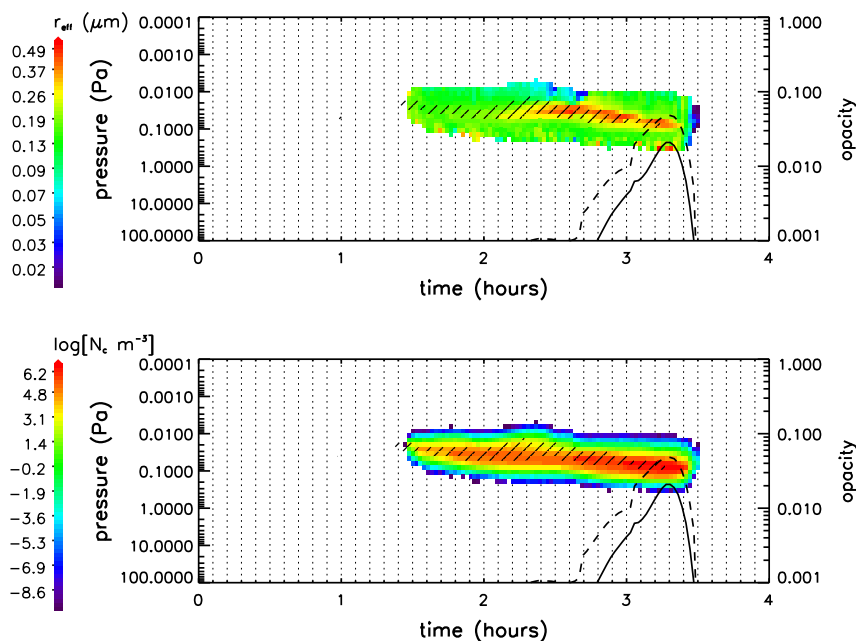


Fig. 14. Crystal effective radius (top) and crystal number density (bottom) for a day cloud obtained with $\Delta T_{\text{shift}} = 1$ K and dust profile D2. Opacity is shown at 1 μm (solid line) and 500 nm (dashed line). Figure axes are as in Fig. 9. Shaded area indicates supersaturated area ($S > 1$). (For interpretation of the references to color in this figure legend, the reader is referred to the web version of this article.)

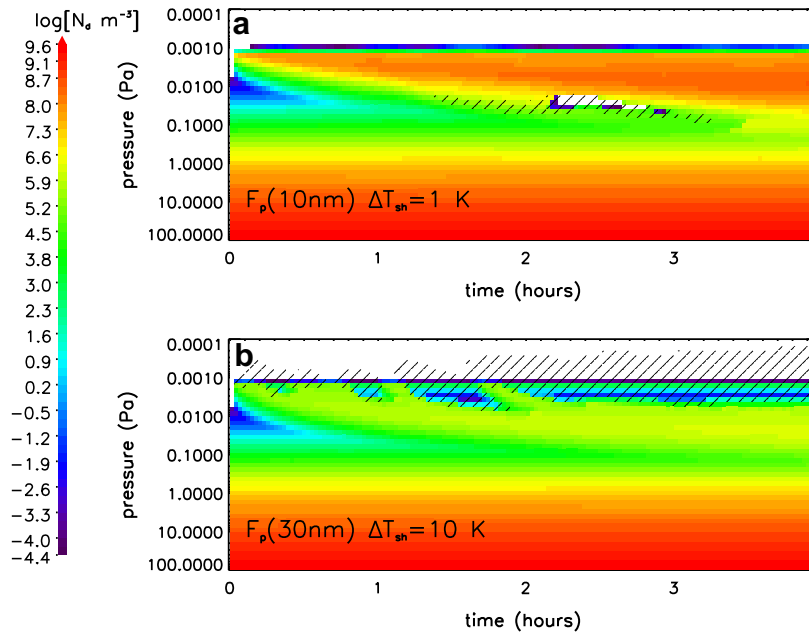


Fig. 15. Dust number density (m^{-3} , colors) as a function of elapsed time (h) with the addition (to the D0 equilibrium profile) of (a) 10 nm particles falling in the daytime supersaturated area and (b) 30 nm particles in the nighttime supersaturated area. Plot (a) corresponds to the simulation shown in Fig. 16 while plot (b) corresponds to the simulation shown in Fig. 18. Figure axes are as in Fig. 9 except that no opacity is shown. (For interpretation of the references to color in this figure legend, the reader is referred to the web version of this article.)

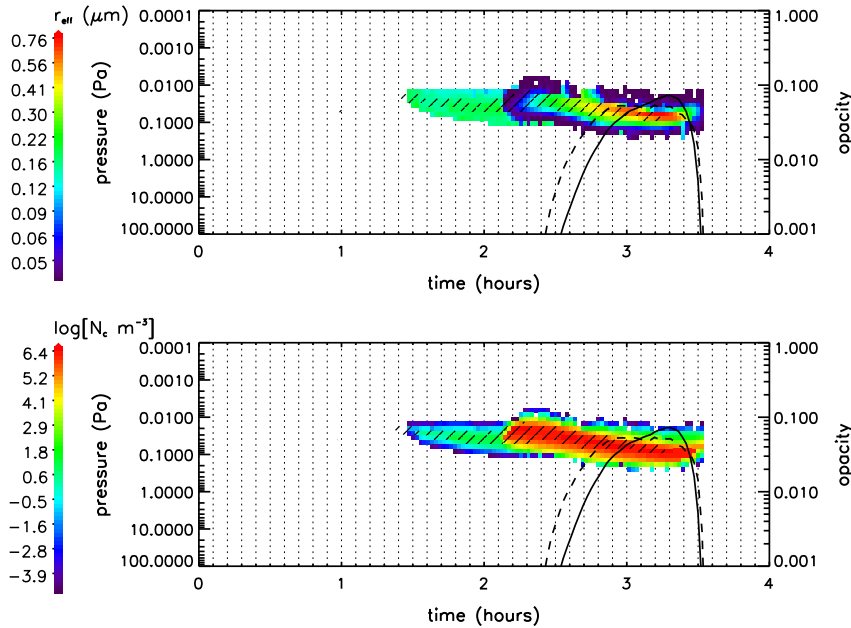


Fig. 16. Crystal effective radius (μm , top) and Crystal number density (in m^{-3} log-scale, bottom) versus elapsed time (in hours) with $\Delta T_{\text{shift}} = 1 \text{ K}$, where a constant source flux $F_p(10 \text{ nm})$ of particles is falling in the supersaturated region as shown in Fig. 15a. Figure axes are as in Fig. 9. Shaded area indicates supersaturated area ($S > 1$). (For interpretation of the references to color in this figure legend, the reader is referred to the web version of this article.)

condensational growth, so that opacity increases up to $\tau \sim 0.08$. After the cold pocket has vanished, the cloud's opacity is decreased by an order of magnitude within ~ 10 min, and by two orders of magnitude within the following few minutes. With $\Delta T_{\text{shift}} = 0 \text{ K}$ the maximum effective radius is $\sim 500 \text{ nm}$, and opacity is 0.02–0.04. The maximum amount of ice forming is $dq_{\text{ice,max}} \sim 10^{-3}$ and $dq_{\text{ice,max}} \sim 3 \cdot 10^{-4}$, by respectively using $\Delta T_{\text{shift}} = 1 \text{ K}$ and $\Delta T_{\text{shift}} = 0 \text{ K}$, so that the trace-gas approximation is only approximately valid for the former case (see also Table 2).

If particles of 10 nm are added lower in altitude, within the area of condensation (as was done for the 1 nm particles), instead of falling from the overlaying atmospheric layers, they are available in increasing concentrations at each time step within the condensation area. This leads to massive crystal formation and consequent vapor loss so that our trace-gas scheme will not be valid. Prescribing a lower production rate allows to remain within the validity limits of the model but would not allow to reach opacities as high as 0.1.

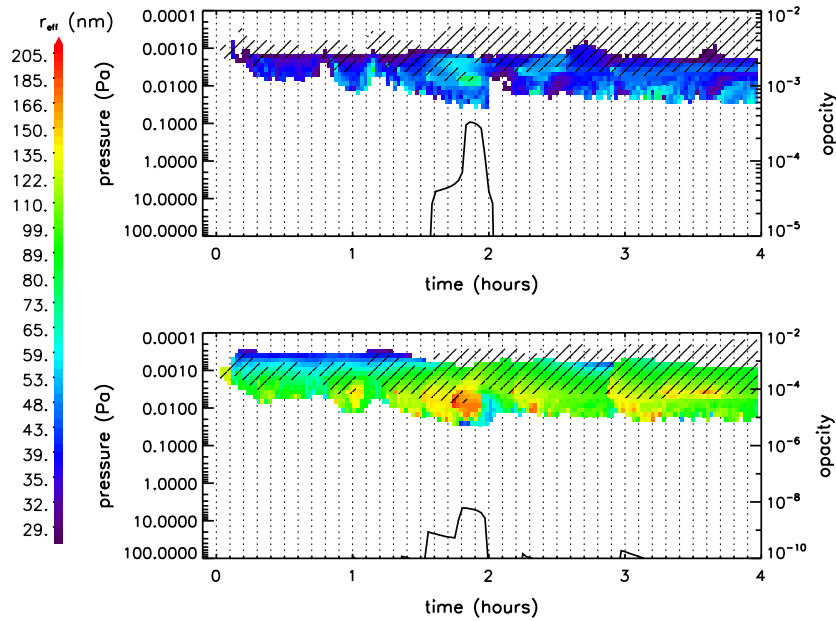


Fig. 17. Effective radius (nm) of nighttime cloud, as a function of elapsed time (hours), obtained with $\Delta T_{\text{shift}} = 10$ K, using D3 dust profile (top) and D0/5000 (bottom). Figure axes are as in Fig. 9. Shaded area indicates supersaturated area ($S > 1$), and corresponds to saturation ratios plotted in Fig. 8b. (For interpretation of the references to color in this figure legend, the reader is referred to the web version of this article.)

4.3.3. Opacities of nighttime clouds

Typical dust content is by far insufficient to reach opacities of nighttime clouds (~ 0.01). Thus, we now use the equilibrium dust profile D3, corresponding to the largest dust load among our scenarios, and use it with $\Delta T_{\text{shift}} = 10$ K. The maximum opacity reached is $\tau \sim 10^{-4}$ (Fig. 17, top), i.e. two orders of magnitude below the average value measured by SPICAM (the lowest measured opacity being $6 \cdot 10^{-3}$). The effective radii obtained along with the corresponding opacity are similar to D0 (~ 80 nm). Dust profile $k_d = 5000 \text{ m}^2 \text{ s}^{-1}$ (D0/5000) allows to

reach larger ice effective radii (Fig. 17, bottom) than D0 (Fig. 10). The reason is that the initial sizes of growing crystals are larger due to larger dust nuclei, and since the condensation process is not efficient at these high altitudes (large Knudsen numbers) the radius of the CN has a large impact on the final crystal size. However, opacities remain much lower ($\tau \leq 10^{-8}$) compared to the case with the D3 profile (Fig. 17, bottom). As for daytime clouds a more efficient vertical mixing does not allow to increase the average dust content enough to get close to observed opacities.

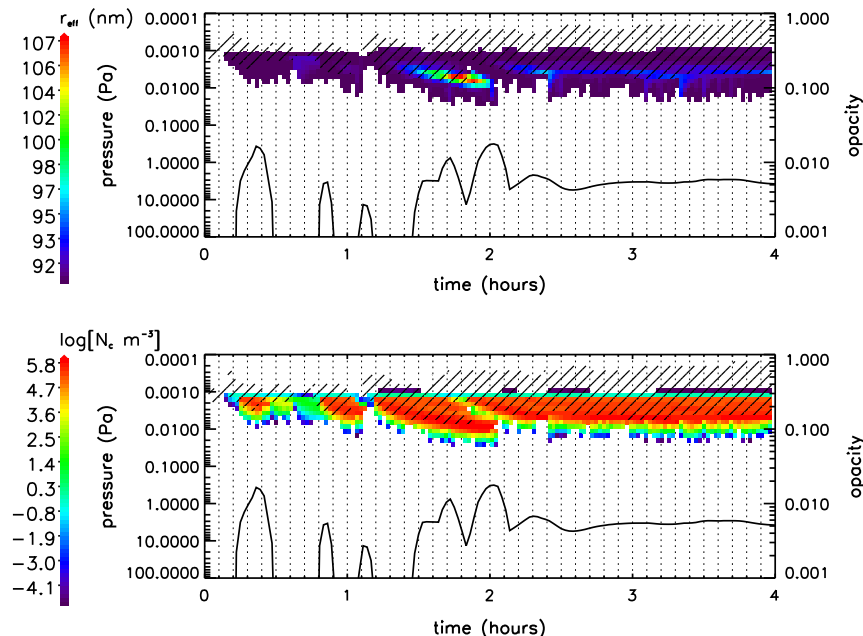


Fig. 18. Crystal effective radius (nm, top) and Crystal number density (in m^3 log-scale, bottom) versus elapsed time (in hours) for a nighttime cloud ($\Delta T_{\text{shift}} = 10$ K). A constant flux of particles $F_p(30 \text{ nm})$ is added to the reference D0 equilibrium dust profile as shown in Fig. 15b. Figure axes are as in Fig. 9. Shaded area indicates supersaturated area ($S > 1$), and corresponds to saturation ratios plotted in Fig. 8b. (For interpretation of the references to color in this figure legend, the reader is referred to the web version of this article.)

Table 2

Summary of simulation results discussed in Section 4. S_{\max} corresponds to the maximum saturation ratio reached where the cloud forms. We show whether or not the trace-gas approximation defined in Section 2.3 is valid ($dm_a/m_a \leq 1\%$) with a checkmark (✓); some results where the trace-gas approximation is only approximately (\sim) valid are shown. The upper part of each (day or night) panel is dedicated to dust average conditions scenario (D0); the bottom part to dustier scenarios. Corresponding figures are indicated. D2/D3 refers to intermediate dust profile between D2 and D3 (Fig. 3b). Due to mass conservation the fluxes $F_p(30\text{ nm})$ and $F_p(50\text{ nm})$ are smaller than $F_p(10\text{ nm})$ by a factor of ~ 30 and ~ 100 respectively. (See section 4.3.1 for the definition of fluxes)

Dust scenario	ΔT_{shift} (K)	S_{\max}	Opacity, τ_{\max}	Radius, r_{eff}	$dm_a/m_a \leq 1\%$	Fig.
<i>Daytime clouds</i>						
D0	0	10	10^{-6}	0.35 μm	✓	–
D0 + [RAD]	0	10	10^{-6}	0.3 μm	✓	–
D0	5	70	10^{-5}	1.3 μm	✓	9
D0 + [RAD]	5	70	10^{-5}	0.55 μm	✓	13 (bottom)
D0 + [RAD]	10	600	10^{-4}	>1 μm	✓	–
D0/5000	5	70	0.002	1 μm	✓	–
D1	5	70	0.004	1.4 μm	✓	–
D2	1	15	0.01–0.05	0.5 μm	✓	14
D2/D3	2	20	0.1	0.7 μm	$\sim(5\%)$	–
$F_p(10\text{ nm})$	0	10	0.01–0.05	0.5 μm	✓	–
$F_p(10\text{ nm})$	1	15	0.05–0.08	0.8 μm	$\sim(3\%)$	16
<i>Nighttime clouds</i>						
D0	5	30	$<10^{-10}$	50 nm	✓	–
D0	10	300	$<10^{-10}$	75 nm	✓	10
D0/5000	10	300	10^{-6}	150–200 nm	✓	17 (bottom)
D3	10	300	0.001	80 nm	✓	17 (top)
D3	12	700	0.004	75 nm	✓	–
$F_p(1\text{ nm})$	10	1000	10^{-5}	5 nm	✓	–
$F_p(10\text{ nm})$	10	300	0.06	80 nm	$\sim(3\%)$	–
$F_p(10\text{ nm})$	12	700	0.1	100 nm	$\sim(6\%)$	–
$F_p(30\text{ nm})$	10	300	0.02	110 nm	✓	18
$F_p(50\text{ nm})$	10	300	0.03	160 nm	✓	–

We investigate the second approach of adding a constant production rate of (meteoric) particles within the ablation altitude range ($<100\text{ km}$). Adding the flux of 1 nm particles $F_p(1\text{ nm})$, whatever the altitude of dust release is (with $\Delta T_{\text{shift}} = 10\text{ K}$), leads to a very small $r_{\text{eff}} (\leq 5\text{ nm})$. Opacity reaches 10^{-5} at maximum where an abundant population of particles of radius $\sim 5\text{ nm}$ is obtained (not shown), and where S reach values above 500 and up to 1000. Using the production rate $F_p(10\text{ nm})$ added over the D0 dust profile, with $\Delta T_{\text{shift}} = 10\text{ K}$, a cloud forms with effective sizes reaching $\sim 70\text{ nm}$ and a maximum crystal number density of $10^7 - 10^8\text{ particles m}^{-3}$ (not shown). If we use a population of 30 nm nuclei with $F_p(30\text{ nm}) \sim F_p(10\text{ nm})/30$ (applying mass conservation, see Section 4.3.1) we simulate a cloud shown in Fig. 18 where r_{eff} reaches $\sim 110\text{ nm}$, the average crystal size measured by Montmessin et al. (2006), and the crystal number density reaches 10^6 m^{-3} . Fig. 15b shows the depletion of dust population due to activation of dust particles as CN. Larger crystal effective radii can be reached by adding larger dust nuclei, for instance a supply of 50 nm particles will lead to crystal radii $\sim 160\text{ nm}$, the largest size measured for nighttime clouds when taking into account retrieval errors (Montmessin et al., 2006). The saturation ratio S reaches ~ 100 at the altitude where the larger radii form. The trace gas approximation remains valid fore most of the cases where the observed r_{eff} and τ are reproduced (Table 2).

In Fig. 18 opacities reach values slightly above 0.02 around 2 h which is close to the maximum opacity derived by SPICAM (Montmessin et al., 2006). The main part of the cloud again evolves in a sub-saturated area (see Fig. 11b, which corresponds to the cloud shown in Fig. 18). This configuration is determined by the temporal pattern of the gravity wave. As for day clouds, the lifetime of the cloud is short once the cold pocket has vanished ($\sim 10\text{ min}$).

Importantly, a constant source of particles forming in the ablation area ($\leq 100\text{ km}$) allows also for a permanent layer of ice particles to remain very close and below the main supersaturated region, due to sedimentation (see at $t > 2.2\text{ h}$ in Fig. 18). This also leads to a configuration where crystals stand below a supersaturated

region with opacities ~ 0.005 , the lowest measured opacities (Montmessin et al., 2006). Crystal number densities are on average lower ($\sim 10^4\text{ m}^{-3}$) than in the supersaturated area ($\sim 10^6\text{ m}^{-3}$). Sedimentation brings the crystals in the subsaturated region where they evaporate fast by falling into warmer layers: only a constant supply of meteoritic dust nuclei can maintain such a configuration, where ice crystals stand below the supersaturated layer responsible for their formation.

5. Discussion

5.1. The role of gravity waves in shaping CO_2 clouds

Whether by day or by night, it is possible to model effective radii of CO_2 ice cloud crystals in agreement with observations (Table 1), with saturation ratios expected in the martian mesosphere. Table 2 summarizes the simulation results previously discussed in the text. Opacities remain far below observed values (by several orders of magnitude) if no dust particles are added on top of what we consider as average conditions during observation epochs of CO_2 clouds (D0 profile). An additional source of condensation nuclei causes the formation of optically thicker clouds. It is possible to get close to (day case) or to reproduce (night case) the typical cloud opacity by prescribing simple dust scenarios (see bottom parts of day and nighttime clouds panels in Table 2). A typical gravity wave causing saturation ratios of ~ 10 –60 is needed to reach sizes of 0.5–2 μm at altitudes around 70–80 km. A typical gravity wave causing saturation ratios S reaching ~ 100 allows for the growth of ice crystals up to $\sim 100\text{ nm}$ at altitudes $\sim 90\text{ km}$. First tests, which were presented in Section 3.3 and Fig. 7 show that different characteristic radii are reached depending mainly on the investigated altitudes, due to different condensation efficiencies in a more or less rarefied atmosphere. The size of the CN (the initial size of the crystal) has also an impact on the final crystal size in simulations (see last rows of Table 2), due to the inefficient condensation process. The values obtained with idealized cold pockets

and with gravity waves are in accordance. However, the more complex temporal/spatial behavior of the gravity wave allows to draw a more precise picture of the formed clouds.

The spatiotemporal propagation of the gravity waves determines the spatiotemporal behavior of the cloud. As an example the shift observed between supersaturated regions and clouds by Montmessin et al. (2006) could be explained by a double peak structure in temperature due to wave propagation (Fig. 11). It is not the sedimentation of the cloud which brings the crystals out of the cold pocket where they have formed. It is instead the cold pocket responsible for the cloud formation that vanishes and leaves the cloud in subsaturated air. This so-to-speak secondary cold pocket stands below a more persistent one in our examples. Profiles published by Montmessin et al. (2011) also show for at least two observations such a secondary lower cold pocket (see observations 0975A1 and 1030A1 in their Fig. 2). The published observations of nighttime clouds suggest that the current detection limit for the CO₂ ice clouds lies around ~ 0.005 in opacity. It is also possible that a population of crystals persist in the atmosphere just below supersaturated layers, with opacities at or below the detection limit as shown in Fig. 18 (after the opacity peak at ~ 2 h). Crystals form into the supersaturated area, fall in warmer layers below, and evaporate. The presence of such a crystal population relies on the presence of a constant CN supply to the atmosphere.

5.2. Impact of radiative heating

The radiative heating of daytime crystals (at ~ 70 – 80 km) requires a large cooling of the atmosphere ($S \sim 600$) to simulate micrometric effective radii, otherwise obtained without the radiative heating terms (Fig. 13). This leads to saturation ratios not expected at the altitudes of daytime clouds (several hundreds see Table 2). On the other hand, radiative cooling of daytime crystals does not significantly affect the effective radius; released latent heat is mostly lost by heat conduction. Higher altitude nighttime crystals are not affected by radiative transfer as we model it, due to their small sizes. A better estimation of the impact of the radiative environment on daytime crystals would be achieved by implementing a full radiative transfer code precisely accounting for the solar, and atmospheric and surface contributions.

5.3. The trace gas approximation

The clouds modeled in agreement with observations respect our trace-gas approximation, $|dq_{\text{ice,lim}}| \sim 3 \cdot 10^{-4}$. This limit corresponds to a total heating of $\delta T_{\text{lim}} \sim 0.25$ K (Section 2.3) and to an energy e_{lim} of 180 J kg^{-1} . However, this value is reached over many time steps during cloud formation, so that the heating of the atmosphere by CO₂ condensation is typically $\sim 0.01 e_{\text{lim}}$ per time step. It appears very likely that latent heat release from CO₂ condensation in the mesosphere does not buffer the amplitude of the temperature perturbation at least for some of the observed clouds, and especially for the nighttime clouds. This is in line with the suggestion of Montmessin et al. (2006) that vertical propagation of waves would be only partly buffered by the release of latent heat induced by nighttime cloud formation.

5.4. Duration of CO₂ clouds and wave activity

Observable CO₂ ice clouds (with $\tau \gtrsim 0.01$) last a short time (~ 10 – 30 min) after the supersaturated region where they form vanishes. The characteristic time scale of cloud formation is less than the characteristic time scale of the gravity wave. Thus, every cloud detection implies a simultaneous cold pocket created by a gravity wave event (but not vice versa).

Creasey et al. (2006) have shown with radio occultation measurements below 30 km altitude that gravity wave activity on Mars is constrained between -20°N and $+20^\circ\text{N}$, i.e. in regions where CO₂ mesospheric clouds are observed. This result shows that a strong wave activity does exist (at least in the troposphere) in regions where gravity waves are theoretically able to propagate up to the mesosphere according to modeling results (Spiga et al., 2012). Works of Creasey et al. (2006) and Spiga et al., (2012) support the idea that gravity waves and mesospheric CO₂ ice cloud formation are closely linked; our simulations are in line with this idea. Because the simulated clouds do not survive a long time in a subsaturated air, and provided that gravity waves are indeed mandatory to create supersaturated pockets in the mesosphere, the abundant gravity wave activity (Creasey et al., 2006) is needed during the season of CO₂ cloud observations, in order to explain abundant detections of these clouds by OMEGA and CRISM.

Finally, the short lifetime of clouds in subsaturated conditions can explain why only in a very few cases, night clouds have been detected in the supersaturated profiles derived by SPICAM (Montmessin et al., 2006, 2011; Forget et al., 2009), although a lack of condensation nuclei (e.g. meteoritic supply) can also explain the absence of a (detectable) cloud (as suggested by results with typical dust profiles shown in Section 4.1.2).

5.5. Clouds precursors

5.5.1. Dust storms

The vast majority of daytime CO₂ ice clouds have been reported in the equatorial region between $L_s = 0^\circ$ and $L_s = 140^\circ$ so far, with an intense peak of formation observed between $L_s = 0^\circ$ and $L_s = 45^\circ$ (Määttänen et al., 2010; Vincendon et al., 2011), and a second peak observed between $L_s = 90^\circ$ and $L_s = 140^\circ$. Detections seem to occur more scarcely between $L_s = 45^\circ$ and $L_s = 90^\circ$ and after $L_s = 180^\circ$. Several mesospheric clouds have been observed around $L_s = 250^\circ$ at mid-latitudes (McConnochie et al., 2010) but the composition of the crystals remains ambiguous. Dust storms might act as a significant source for CN. We showed that enhanced dust loading typical for dust storm periods (dust profiles D1–D3) can help to bring the simulated opacities of clouds closer to the observed ones (Section 4.3.2, Fig. 14 and Table 2). The main dust storm season on Mars occurs around $L_s = 270^\circ$. A dust storm has been observed in MY 28 encircling the planet between $L_s = 265^\circ$ and 310° (Smith, 2009). MY29 showed a strong activity peak in CO₂ ice cloud formation between $L_s = 0^\circ$ and 36° (with two isolated cases at $L_s = 87^\circ$ and $L_s = 330^\circ$) with OMEGA (Määttänen et al., 2010) and between $L_s = 15^\circ$ and $L_s = 138^\circ$ with CRISM (Vincendon et al., 2011). This might be partly explained by a replenishment of the atmosphere with a significant amount of dust to help detectable clouds to form. However, typical residence time (time for falling one scale height i.e. ~ 10 km) for a 10 nm dust particle lies between 1 h (at 100 km) and 10 sols (at 60 km), for a 100 nm particle it is < 1 sol. Dust storms alone cannot act as a long-term persistent CN source at altitudes where clouds are observed. Detections of dust detached layers have been made at altitudes 15–25 km by night (Heavens et al., 2011b) and during the day at altitudes 45–60 km (Guzewich et al., 2013), outside the dust storm season. Recent modeling studies suggest that strong vertical injection of dust could create similar layers in the troposphere (Spiga et al., 2013). However, it remains unclear how such mechanisms could supply the high mesosphere with abundant condensation nuclei for the CO₂ clouds to form.

5.5.2. Meteoric particles

Another source is presumably needed to explain the measured opacities along the whole period of CO₂ cloud observations. The alternative source that has been investigated is the constant deposition of meteoritic material from the interplanetary medium,

known as IDPs (Interplanetary Dust Particles). We believe this could be a key for the understanding of the formation of mesospheric clouds on Mars, as it was suggested for mesospheric clouds on Earth (Turco et al., 1981; Rapp and Thomas, 2006). In Section 4.3 we prescribed a constant flux of falling particles to account for meteoric supply of condensation nuclei. This helped to simulate the observed opacities of CO₂ clouds in the mesosphere where meteoroids should ablate (Adolfsson et al., 1996). For meteoric input in the martian mesosphere we have taken the estimation of Flynn (1992). Interestingly, a more recent study dealing with the modeling of the zodiacal cloud (Nesvorný et al., 2010) estimate the quantity of accreted IDPs by Earth, Moon and Mars. On the latter it is estimated to be 1.6×10^7 kg per year (20% of Earth's flux). According to Flynn (1992), one sixth of material is expected to vaporize and recondense. Thus Nesvorný et al. (2010)'s flux gives a CN-source of $\sim 10^6$ kg per year: a similar order of magnitude estimate than obtained by Flynn (1992). Observational evidence for meteoric activity in the martian mesosphere was reported by Pätzold et al. (2005), Withers et al. (2008) and Pandya and Haider (2012) through detection of recurrent enhancement in electron density between ~ 70 –100 km. These observations had been first predicted by models (Molina-Cuberos et al., 2003). Electrons are produced through ionization of metallic atoms coming from meteoroid ablation. Observation of meteoric electronic layers are an additional hint that the actual ablation altitudes correspond to the altitude range where CO₂ clouds form.

Hunten et al. (1980) and Bardeen et al. (2008) have estimated concentrations of recondensed particles in the terrestrial mesosphere with the help of 1D- and 3D-modeling respectively. Both agree on the possibility to have nanoparticles at concentration around 10^9 m⁻³ in the high mesosphere. Bardeen et al. (2008) showed that upward winds could allow for particles with sizes reaching ~ 5 –10 nm to remain in the high mesosphere at concentrations 10^6 m⁻³. The shape of IDP also influence the altitude where it ablates: for instance fractal particles will ablate less and at higher altitudes on Earth (~ 100 km instead of ~ 80 km, Kalashnikova et al. (2000)). Similar mechanisms could occur on Mars, although ablation is less efficient because of lower densities, letting more material to reach the surface without evaporation during atmospheric entry (Flynn and McKay, 1990).

Regarding densities for IDPs, Jessberger et al. (2001) suggests a value of 2500 kg m⁻³. Nesvorný et al. (2010) use 2000 kg m⁻³, although other investigators suggest 1000 kg m⁻³ for cometary grains (Wiegert et al., 2009). Although there is no reason that meteoric smoke particles conserve their material density upon ablation/recondensation, Hunten et al. (1980), Kalashnikova et al., 2000 and Bardeen et al., 2008 respectively use 2000 kg m⁻³ and 2500 kg m⁻³ for these particles. We use 2500 kg m⁻³ as it is similar to the average martian dust density. Using $\rho \sim 1000$ kg m⁻³ does not change the order of magnitude estimates of fluxes F_p (Section 4.3.1) and does not affect our results.

5.5.3. Water ice clouds

Another source of potential nuclei are water ice clouds, some of which have been identified at similar locations than CO₂ clouds, but at lower altitudes (≤ 60 km, Heavens et al. (2011a)). In a limb observation of a water ice cloud by OMEGA (Vincendon et al., 2011), the number density of water ice decreases from bottom to top of the cloud (M. Vincendon, personal communication, 2011), possibly suggesting that the icy particles could have been transported upward (by atmospheric dynamics). Note that water ice clouds would also need condensation nuclei to form. According to our estimations homogeneous nucleation of water ice at mesospheric altitudes (≥ 50 km, or ~ 1 Pa) requires saturation ratios above at least 10^5 . Supersaturations of water vapor measured so far on Mars (Maltagliati et al., 2011) preclude us from considering

the possibility of homogeneous nucleation of water ice. A supply (by upward mixing) of water ice condensates from lower altitudes to altitudes where CO₂ ice clouds can form is a scenario that requires further investigation.

5.5.4. Other scenarios?

Electronic layers originating from meteoroid ablation and detected in the martian mesosphere (Pätzold et al., 2005; Withers et al., 2008) could also participate in charging mechanisms involving dust or meteoric particles. Charged aerosols were suggested by Gumbel and Megner (2009) as very efficient precursors for PMCs formation on Earth. This remains to be explored for cloud formation on Mars.

Also, the role of the magnetic field in particle suspension have been addressed on Earth, at the poles, where the vertical magnetic field lines would allow for suspension of magnetized particles in the terrestrial mesosphere (Rohatschek and Horvath, 2010; Cheremisin et al., 2011). Micrometeorites are known to have ferromagnetic inclusions which make them sensitive to magnetic fields, and martian dust is known to have strong magnetic properties (see e.g. Leer et al., 2011). Observations of various geometries of pitch angle distributions of electrons measured by Mars Global Surveyor suggest varying geometries for magnetic field lines on Mars (Brain et al., 2007), caused by interactions between the residual magnetic field (Acuña et al., 1999; Acuña et al., 2001; Mitchell et al., 2005) and interplanetary magnetic field. Whether interactions between vertical magnetic field lines and particles could occur on Mars, as suggested for Earth (Rohatschek and Horvath, 2010; Cheremisin et al., 2011), remains unknown.

Thus, our study calls mainly for more experimental constraints on meteoric flux into the martian atmosphere.

6. Conclusion and perspectives

We have presented for the first time a model of CO₂ ice cloud formation within mesospheric cold pockets on Mars, created by gravity wave propagation. We have shown that mesospheric cloud evolution is essentially governed by the cold pocket temporal and spatial behavior, which causes the formation of clouds bearing similarities with the observed CO₂ clouds, inasmuch as observational evidence is available (the time evolution of a single cloud not having been constrained yet). Also, meteoric particles appear as relevant (and necessary) cloud precursors to explain the measured opacities of clouds, along their whole period of observation. However, measurements of meteoric dust fluxes remain necessary to better constrain scenarios implying such exogenic supply of nuclei. We have shown that it is important to use a model adapted to high supersaturations of CO₂ (Listowski et al., 2013) to correctly model the cloud lifetime, vertical extent, and opacities, as well as the effective radii of crystals.

More investigation has to be done since only CO₂ clouds above ~ 70 km have been modeled in this study. A complete picture of CO₂ mesospheric cloud modeling demands to address the case of the lowest altitudes observed for CO₂ clouds (≥ 55 km, see Scholten et al., 2010; Määttänen et al., 2010). Moreover the optically thickest clouds ($r_{\text{eff}} > 1$ μm and $\tau > 0.1$) are not within the reach of our model and remain to be properly simulated.

Furthermore, recent modelling studies on Earth have shown the critical link between PMCs brightness and gravity waves (Chandran et al., 2012). For martian CO₂ clouds, further insights would be achieved by interfacing our CO₂ ice microphysics with a 3D Mars Mesoscale Model (Spiga and Forget, 2009), where interactions between clouds and dust will be better constrained, and where 3D atmospheric dynamics will allow for more realistic modeling of cloud evolution through horizontal transport and horizontal propagation of gravity waves.

Acknowledgments

We wish to thank an anonymous reviewer for the very careful reading of the paper and for suggestions which help to improve and clarify the manuscript.

Appendix A. Derivation of simplified radiative heat transfer contributions to the energy budget of the crystal: P_{cool} , P_{sol} and P_{atm}

The radiative cooling term, P_{cool} , is derived as follows:

$$P_{cool}(r, T_a) = 4\pi r^2 \int_0^\infty Q_{abs}(\lambda, r) B_\lambda(T_a) d\lambda, \quad (\text{A.1})$$

where r is the crystal radius, λ the wavelength, and $B_\lambda(T)$ is given by Planck's law. The absorption efficiency $Q_{abs}(\lambda, r) = \sigma_{eff,abs}(\lambda, r)/(\pi r^2)$, where $\sigma_{eff,abs}$ is the absorption cross-section efficiency, is derived from CO₂ ice optical constants given by Hansen (1997, 2005). The term $4\pi r^2$ is due to the fact that the entire crystal surface radiates.

The solar heating term, P_{sol} , is derived as follows:

$$P_{sol}(r) = \pi r^2 \times \left(\frac{R_\odot}{d_{Sun/Mars}} \right)^2 \times \int_0^\infty Q_{abs}(\lambda, r) B_\lambda(T_\odot) d\lambda, \quad (\text{A.2})$$

where R_\odot is the sun radius ($\sim 696,000$ km), T_\odot its effective temperature (~ 5800 K), and $d_{Sun/Mars}$ is the mean Mars–Sun distance. The πr^2 factor is due to the fact that we consider an ideal case where the solar flux intersects the front section of the crystal (no absorption from secondary sources).

Atmospheric heating term (including surface contribution), P_{atm} , is derived as follows:

$$P_{atm}(r, T_{eff}) = 2\pi r^2 \int_0^\infty Q_{abs}(\lambda, r) B_\lambda(T_{eff}) d\lambda, \quad (\text{A.3})$$

T_{eff} is the effective temperature extracted from the infrared flux to space, F_{IR} , taken as a black-body (from Stefan–Boltzmann law $F_{IR} = \sigma_{SB} T_{eff}^4$ with $\sigma_{SB} \sim 5.7 \times 10^{-8}$ W m⁻² K⁻⁴ the Stefan-Boltzmann constant). F_{IR} is given by the Martian Climate Database (MCD, Millour et al., 2008). P_{atm} is multiplied by $2\pi r^2$ since we consider that the crystal intersects a flux coming from a 2π solid angle (the bottom hemisphere of the crystal).

In the following we explain the method to obtain more compact expressions for these terms, which are simplified estimations of the radiative heat transfer contribution to the crystal energy budget (see discussion in Section 4.1.3). The power laws we obtain for these expressions are useful especially for the cooling term whose derivative is needed for implementation in the Newton–Raphson routine we use to iteratively solve for T_a . The iterative process applies for the surface temperature of the crystal, T_a , on which P_{cool} depends.

Regarding this radiative cooling term we plotted $\ln P_{cool}$ versus radius $\ln r_{\mu m}$ for a temperature range going from $T_a = 60$ K to $T_a = 150$ K (approximately the CO₂ condensation temperature at the martian surface). We were able to fit a linear regression of the form:

$$\ln P_{cool} = a(T_a) + b(T_a) \ln r_{\mu m}, \quad (\text{A.4})$$

where $a(T_a)$ and $b(T_a)$ are fitting parameters determined for each T_a value (0.5 K increment). We proceed in this way for three distinct radius ranges to minimize errors in the fits on the entire radius range (1 nm to 100 μm). Examples of fits are shown in Fig. A.1 with a 10 K step, from 60 K to 150 K. Then, analytical formulas for $a(T_a)$ and $b(T_a)$ could be obtained by using the arctan function (Fig. A.2). We constrain the fits to the range $T_a = 70$ –140 K, which helps improving the match between data and model for both $a(T_a)$ and $b(T_a)$. Surface temperatures of crystals during runs were always contained within this range. Values below 70 K were found for exceptional cases (very

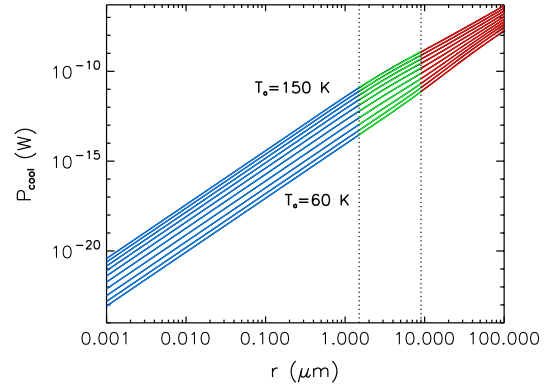


Fig. A.1. Plots and (superposed) fits of the radiative cooling term $P_{cool}(r)$, on a log–log scale, as a function of the crystal radius r . Plots are shown for different values of crystal surface temperature T_a : from 60 K to 150 K (plotted with a 10 K step). The three colors are related to the three different radius ranges, which are distinguished for fitting (see Table A.1). (For interpretation of the references to color in this figure legend, the reader is referred to the web version of this article.)

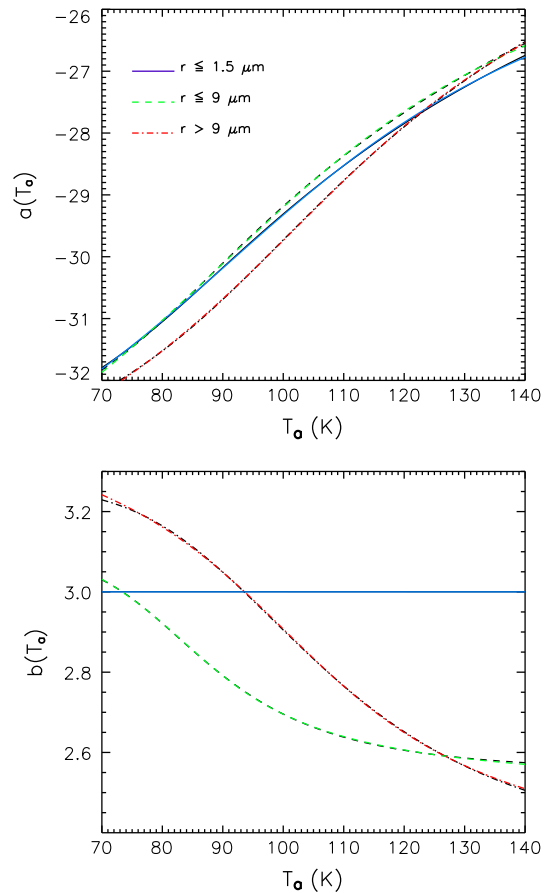


Fig. A.2. Coefficients $a(T_a)$ and $b(T_a)$ of Eq. (A.4) as a function of T_a (black), and their respective fits (superposed in color) for three distinct radius ranges. Analytical formulae used for fitting are given by Eq. (A.5). (For interpretation of the references to color in this figure legend, the reader is referred to the web version of this article.)

low concentrations $<10^{-10}$ m⁻³ or rare situations where crystals were evolving in very sub-saturated areas with $S \leq 10^{-4}$). Maximum temperatures at crystal surface in our mesospheric simulations are ~ 110 K, but we keep the temperature range up to 140 K to encompass surface temperatures of crystals at the poles.

Table A.1

Coefficients related to power-laws used for the three radiative terms.

Coeff.	Radiative cooling		
	if $r \leq 1.5 \mu\text{m}$	if $r \leq 9 \mu\text{m}$	Else
q_1	4.16	4.29	4.08
q_2	91.2	89.7	101.88
q_3	47.9	46.2	41.9
q_4	−30.08	−30.14	−29.554
q_5	0	−0.2410	−0.407
q_6	0	83.49	100.37
q_7	1	17.84	27.5
q_8	3	2.8753	2.902
Solar heating			
	if $r \leq 300 \text{ nm}$	if $r \leq 3 \mu\text{m}$	Else
$\ln k_s$	−26.36	−26.73	−26.38
z_s	2.99	2.67	2.33
Combined atmospheric/surface heating (MAX)			
	if $r \leq 1.2 \mu\text{m}$	if $r \leq 3.4 \mu\text{m}$	Else
$\ln k_a$	−25.93	−25.90	−25.43
z_a	3.0	2.76	2.38
Combined atmospheric/surface heating (MIN)			
	if $r \leq 1 \mu\text{m}$	if $r \leq 3.5 \mu\text{m}$	Else
$\ln k_a$	−24.30	−24.29	−23.76
z_a	3.0	2.77	2.35

This results in the following coefficients for the radiative cooling:

$$a(T_a) = q_1 \arctan\left(\frac{T_a - q_2}{q_3}\right) + q_4 \quad (\text{A.5})$$

$$b(T_a) = q_5 \arctan\left(\frac{T_a - q_6}{q_7}\right) + q_8,$$

where the q_i coefficients are given in Table A.1. Thus, we have, by letting $k_c(T_a) = \exp[a(T_a)]$ and $z_c(T_a) = b(T_a)$:

$$P_{cool}(r, T_a) = k_c(T_a) r_{\mu\text{m}}^{z_c(T_a)}. \quad (\text{A.6})$$

Note that here we have an analytical expression of P_{cool} , from which the derivative can easily be obtained as a composition of common functions. For a given radius, r , $P_{cool}(r, T_a)$ is derived with respect to T_a . Errors associated with this idealized power-law (for $T_a = 70$ – 140 K) are always $\leq 1\%$ for $r \leq 1 \mu\text{m}$ and always lower than 5% for $r \leq 80 \mu\text{m}$ (except for 1.2 – $2 \mu\text{m}$ and 8 – $12 \mu\text{m}$ where it ranges from 5% to 9%). Errors are comprised between 10% and 20% for $r = 80$ – $100 \mu\text{m}$.

Similarly, we can obtain compact expressions for P_{sol} and P_{atm} (which however does not rely on crystal surface temperature, but only on crystal radius). Again, three fits are obtained for the three radius ranges used, and P_{sol} is now given by:

$$P_{sol}(r) = k_s r_{\mu\text{m}}^{z_s}, \quad (\text{A.7})$$

where k_s and z_s are given in Table A.1. Errors associated to this formula are $\leq 5\%$, except between 100 and 300 nm where they are in the range 5–8%, and between $2.2 \mu\text{m}$ – μm in the range 5–9%.

For P_{atm} , we extracted from the MCD two cases of minimum and maximum IR flux to space, corresponding respectively to early morning/late afternoon and mid-day (~ 2 pm) typical values for F_{IR} . The highest value for F_{IR} is set to 250 W m^{-2} and the low value to 80 W m^{-2} . Our fitting results in the following expression:

$$P_{atm}(r) = k_a r_{\mu\text{m}}^{z_a}, \quad (\text{A.8})$$

where k_a and z_a are given in Table A.1 for the low emission and high emission case and for distinct radius ranges. Errors associated to this formula are below 3% for $r \leq 1 \mu\text{m}$ and in the range 3–5% for $r > 1 \mu\text{m}$.

References

- Acuña, M.H. et al., 1999. Global distribution of crustal magnetization discovered by the Mars Global Surveyor MAG/ER Experiment. *Science* 284, 790. <http://dx.doi.org/10.1126/science.284.5415.790>.
- Acuña, M.H. et al., 2001. Magnetic field of Mars: Summary of results from the aerobraking and mapping orbits. *J. Geophys. Res.* 106, 23403–23418. <http://dx.doi.org/10.1029/2000JE001404>.
- Adolfsson, L.G., Gustafson, B.A.S., Murray, C.D., 1996. The martian atmosphere as a meteoroid detector. *Icarus* 119, 144–152. <http://dx.doi.org/10.1006/icar.1996.0007>.
- Bailey, M., Hallett, J., 2004. Growth rates and habits of ice crystals between -20° and -70°C . *J. Atmos. Sci.* 61, 514–544. [http://dx.doi.org/10.1175/1520-0469\(2004\)061<0514:GRAHOL>2.0.CO;2](http://dx.doi.org/10.1175/1520-0469(2004)061<0514:GRAHOL>2.0.CO;2).
- Bailey, M., Hallett, J., 2006. Measured ice crystal capacitances: The failure of the electrostatic analogy. In: American Meteorological Society, 12th Conference on Cloud Physics.
- Bardeen, C.G., Toon, O.B., Jensen, E.J., Marsh, D.R., Harvey, V.L., 2008. Numerical simulations of the three-dimensional distribution of meteoric dust in the mesosphere and upper stratosphere. *J. Geophys. Res. (Atmos.)* 113, 17202. <http://dx.doi.org/10.1029/2007JD009515>.
- Blamont, J.E., Chassefiere, E., 1993. First detection of ozone in the middle atmosphere of Mars from solar occultation measurements. *Icarus* 104, 324–336. <http://dx.doi.org/10.1006/icar.1993.1104>.
- Brain, D.A., Lillis, R.J., Mitchell, D.L., Halekas, J.S., Lin, R.P., 2007. Electron pitch angle distributions as indicators of magnetic field topology near Mars. *J. Geophys. Res. (Space Phys.)* 112, 9201. <http://dx.doi.org/10.1029/2007JA012435>.
- Chandran, A. et al., 2012. Atmospheric gravity wave effects on Polar Mesospheric Clouds: A comparison of numerical simulations from CARMA 2D with AIM observations. *J. Geophys. Res. (Atmos.)* 117, 21014. <http://dx.doi.org/10.1029/2012JD017794>.
- Chassefiere, E., Blamont, J.E., Krasnopol'Skii, V.A., Korabiev, O.I., Atreya, S.K., West, R.A., 1992. Vertical structure and size distributions of martian aerosols from solar occultation measurements. *Icarus* 97, 46–69. [http://dx.doi.org/10.1016/0019-1035\(92\)90056-D](http://dx.doi.org/10.1016/0019-1035(92)90056-D).
- Cheremisin, A.A., Shnipov, I.S., Horvath, H., Rohatschek, H., 2011. The global picture of aerosol layers formation in the stratosphere and in the mesosphere under the influence of gravito-photophoretic and magneto-photophoretic forces. *J. Geophys. Res. (Atmos.)* 116, 19204. <http://dx.doi.org/10.1029/2011JD015958>.
- Clancy, R.T., Sandor, B.J., 1998. CO_2 ice clouds in the upper atmosphere of Mars. *Geophys. Res. Lett.* 25, 489–492.
- Clancy, R.T., Wolff, M.J., Christensen, P.R., 2003. Mars aerosol studies with the MGS TES emission phase function observations: Optical depths, particles sizes, and ice cloud types versus latitude and solar longitude. *J. Geophys. Res.* 108, 5098. <http://dx.doi.org/10.1029/2003JE002058>.
- Clancy, R.T., Wolff, M.J., Whitney, B.A., Cantor, B.A., Smith, M.D., 2007. Mars equatorial mesospheric clouds: Global occurrence and physical properties from Mars Global Surveyor Thermal Emission Spectrometer and Mars Orbiter Camera limb observations. *J. Geophys. Res.* 112, E04004. <http://dx.doi.org/10.1029/2006JE002805>.
- Colaprete, A., Toon, O.B., 2003. Carbon dioxide clouds in an early dense martian atmosphere. *J. Geophys. Res.* 108 (E4), 5025. <http://dx.doi.org/10.1029/2002JE001967>.
- Colaprete, A., Haberle, R.M., Toon, O.B., 2003. Formation of convective carbon dioxide clouds near the south pole of Mars. *J. Geophys. Res.* 108 (E7), 5081. <http://dx.doi.org/10.1029/2003JE002053>.
- Colaprete, A., Barnes, J.R., Haberle, R.M., Montmessin, F., 2008. CO_2 clouds, CAPE and convection on Mars: Observations and general circulation modeling. *Planet. Space Sci.* 56, 150–180. <http://dx.doi.org/10.1016/j.pss.2007.08.010>.
- Creasey, J.E., Forbes, J.M., Keating, G.M., 2006. Density variability at scales typical of gravity waves observed in Mars' thermosphere by the MGS accelerometer. *Geophys. Res. Lett.* 33, 22814. <http://dx.doi.org/10.1029/2006GL027583>.
- Feder, J., Russell, K.C., Lothe, J., Pound, G.M., 1966. Homogeneous nucleation and growth of droplets in vapours. *Adv. Phys.* 15, 111–178.
- Flynn, G.J., 1992. The meteoritic contribution to dust and aerosols in the atmosphere of Mars. In: In Lunar and Planetary Inst., Workshop on the Martian Surface and Atmosphere Through Time. pp. 51–52 (SEE N92-28988 19-91).
- Flynn, G.J., McKay, D.S., 1990. An assessment of the meteoritic contribution to the martian soil. *J. Geophys. Res.* 95, 14497–14509. <http://dx.doi.org/10.1029/JB095iB09p14497>.
- Forget, F. et al., 1999. Improved general circulation models of the martian atmosphere from the surface to above 80 km. *J. Geophys. Res.* 104, 24155–24176.
- Forget, F. et al., 2009. The density and temperatures of the upper martian atmosphere measured by stellar occultations with Mars Express SPICAM. *J. Geophys. Res.* 114, E01004. <http://dx.doi.org/10.1029/2008JE003086>.
- Foster, J.L., Chang, A.T.C., Hall, D.K., Wergin, W.P., Erbe, E.F., Barton, J., 1998. Carbon dioxide crystals: An examination of their size, shape, and scattering properties at 37 GHz and comparisons with water ice (snow) measurements. *J. Geophys. Res. (Planets)* 103, 25839–25850. <http://dx.doi.org/10.1029/98JE02493>.
- Fuchs, N.A., Sutugin, A.G., 1971. Highly dispersed aerosols. In: Hidy, G.M., Brock, J.R. (Eds.), Topics in Current Aerosol Research, vol. 2. Pergamon, New York, pp. 1–60.
- Glandorf, D.L., Colaprete, A., Tolbert, M.A., Toon, O.B., 2002. CO_2 snow on Mars and early Earth: Experimental constraints. *Icarus* 160, 66–72.
- González-Galindo, F., Forget, F., López-Valverde, M.A., Coll, M.A., Millour, E., 2009. A ground-to-exosphere martian general circulation model: 1. Seasonal, diurnal

- and solar cycle variation of thermospheric temperatures. *J. Geophys. Res.* 114, E04001. <http://dx.doi.org/10.1029/2008JE003246>.
- González-Galindo, F., Määttänen, A., Forget, F., Spiga, A., 2011. The martian mesosphere as revealed by CO₂ cloud observations and general circulation modeling. *Icarus* 216, 10–22. <http://dx.doi.org/10.1016/j.icarus.2011.08.006>.
- Gumbel, J., Megner, L., 2009. Charged meteoric smoke as ice nuclei in the mesosphere: Part 1 – A review of basic concepts. *J. Atmos. Solar-Terr. Phys.* 71, 1225–1235. <http://dx.doi.org/10.1016/j.jastp.2009.04.012>.
- Guzewich, S.D., Talaat, E.R., Toigo, A.D., Waugh, D.W., McConnochie, T.H., 2013. High-altitude dust layers on Mars: Observations with the Thermal Emission Spectrometer. *J. Geophys. Res. (Planets)* 118, 1177–1194. <http://dx.doi.org/10.1002/jgre.20076>.
- Haider, S.A., Singh, V., Choksi, V.R., Maguire, W.C., Verigin, M.I., 2007. Calculated densities of H₃O⁺(H₂O)_n, NO₂⁺(H₂O)_m, CO₃⁻(H₂O)_n, and electron in the nighttime ionosphere of Mars: Impact of solar wind electron and galactic cosmic rays. *J. Geophys. Res. (Space Phys.)* 112. <http://dx.doi.org/10.1029/2007JA012530>, 12309+.
- Hansen, G.B., 1997. The infrared absorption spectrum of carbon dioxide ice from 1.8 to 333 μm. *J. Geophys. Res.* 102, 21569–21588. <http://dx.doi.org/10.1029/97JE01875>.
- Hansen, G.B., 2005. Ultraviolet to near-infrared absorption spectrum of carbon dioxide ice from 0.174 to 1.8 μm. *J. Geophys. Res. (Planets)* 110, 11003. <http://dx.doi.org/10.1029/2005JE002531>.
- Hanson, W.B., Sanatani, S., Zuccaro, D.R., 1977. The martian ionosphere as observed by the Viking retarding potential analyzers. *J. Geophys. Res.* 82, 4351–4363. <http://dx.doi.org/10.1029/J082i028p04351>.
- Heavens, N.G., McCreese, D.J., Richardson, M.I., Kass, D.M., Kleinböhl, A., Schofield, J.T., 2011a. Structure and dynamics of the martian lower and middle atmosphere as observed by the Mars Climate Sounder: 2. Implications of the thermal structure and aerosol distributions for the mean meridional circulation. *J. Geophys. Res. (Planets)* 116, 1010. <http://dx.doi.org/10.1029/2010JE003713>.
- Heavens, N.G. et al., 2011b. Vertical distribution of dust in the martian atmosphere during northern spring and summer: High-altitude tropical dust maximum at northern summer solstice. *J. Geophys. Res. (Planets)* 116, 1007. <http://dx.doi.org/10.1029/2010JE003692>.
- Hervig, M.E., Deaver, L.E., Bardeen, C.G., Russell, J.M., Bailey, S.M., Gordley, L.L., 2012. The content and composition of meteoric smoke in mesospheric ice particles from SOFIE observations. *J. Atmos. Solar-Terr. Phys.* 84, 1–6. <http://dx.doi.org/10.1016/j.jastp.2012.04.005>.
- Hunten, D.M., Turco, R.P., Toon, O.B., 1980. Smoke and dust particles of meteoritic origin in the mesosphere and stratosphere. *J. Atmos. Sci.* 37, 1342.
- Izakov, M.N., 2007. Turbulence in the free atmospheres of Earth, Mars, and Venus: A review. *Solar Syst. Res.* 41, 355–384. <http://dx.doi.org/10.1134/S0038094607050012>.
- Jacobson, M., Turco, R.P., Jensen, E.J., Toon, O.B., 1994. Modeling coagulation among particles of different composition and size. *Atmos. Environ.* 28, 1327–1338.
- James, P.B., Kieffer, H.H., Paige, D.A., 1992. The seasonal cycle of carbon dioxide on Mars, pp. 934–968.
- Jessberger, E.K. et al., 2001. Properties of interplanetary dust: Information from collected samples. In: Grün, E., Gustafson, B.A.S., Dermott, S., Feghtig, H. (Eds.), *Interplanetary Dust, Astronomy and Astrophysics Library*. Springer, Berlin, p. 253, 804 p. ISBN: 3-540-42067-3.
- Kalashnikov, O., Horányi, M., Thomas, G.E., Toon, O.B., 2000. Meteoric smoke production in the atmosphere. *Geophys. Res. Lett.* 27, 3293–3296. <http://dx.doi.org/10.1029/1999GL011338>.
- Keese, R.G., 1989. Nucleation and particle formation in the upper atmosphere. *J. Geophys. Res.* 94, 14683–14692.
- Korablev, O.I., Krasnopolsky, V.A., Rodin, A.V., Chassefiere, E., 1993. Vertical structure of martian dust measured by solar infrared occultations from the PHOBOS spacecraft. *Icarus* 102, 76–87. <http://dx.doi.org/10.1006/icar.1993.1033>.
- Lazaridis, M., Kulmala, M., Gorbunov, B.Z., 1992. Binary heterogeneous nucleation at a non-uniform surface. *J. Aerosol Sci.* 23, 457–466.
- Leer, K. et al., 2011. RAT magnet experiment on the Mars Exploration Rovers: Spirit and Opportunity beyond sol 500. *J. Geophys. Res. (Planets)* 116, 0. <http://dx.doi.org/10.1029/2010JE003667>.
- Listowski, C., Määttänen, A., Riipinen, I., Montmessin, F., Lefèvre, F., 2013. Near-pure vapor condensation in the martian atmosphere: CO₂ ice crystal growth. *J. Geophys. Res. (Planets)* 118, 2153–2171. <http://dx.doi.org/10.1002/jgre.20149>.
- Määttänen, A. et al., 2005. Nucleation studies in the martian atmosphere. *J. Geophys. Res. (Planets)* 110. <http://dx.doi.org/10.1029/2004JE002308>, 2002+.
- Määttänen, A., Vehkamäki, H., Lauri, I., Napari, I., Kulmala, M., 2007. Two-component heterogeneous nucleation kinetics and an application to Mars. *Jcp* 127, 134710. <http://dx.doi.org/10.1063/1.2770737>.
- Määttänen, A., Montmessin, F., Gondet, B., Scholten, F., Hoffmann, H., González-Galindo, F., Spiga, A., Forget, F., Hauber, E., Neukum, G., Bibring, J., Bertaux, J., 2010. Mapping the mesospheric CO₂ clouds on Mars: MEx/OMEGA and MEx/HRSC observations and challenges for atmospheric models. *Icarus* 209, 452–469. <http://dx.doi.org/10.1016/j.icarus.2010.05.017>.
- Määttänen, A., Pérot, K., Montmessin, F., Hauchecorne, A., 2013. Mesospheric clouds on Mars and on Earth. In: Mackwell, S.J., et al. (Eds.), *Comparative Climatology of the Terrestrial Planets*. Univ. of Arizona, Tuscon, pp. 393–413. http://dx.doi.org/10.2458/azu_uapress_9780816530595-ch16.
- Maltagliati, L., Montmessin, F., Fedorova, A., Korablev, O., Forget, F., Bertaux, J.L., 2011. Evidence of water vapor in excess of saturation in the atmosphere of Mars. *Science* 333, 1868. <http://dx.doi.org/10.1126/science.1207957>.
- McConnochie, T.H., Bell, J.F., Savransky, D., Wolff, M.J., Toigo, A.D., Wang, H., Richardson, M.I., Christensen, P.R., 2010. THEMIS-VIS observations of clouds in the martian mesosphere: Altitudes, wind speeds, and decameter-scale morphology. *Icarus* 210, 545–565. <http://dx.doi.org/10.1016/j.icarus.2010.07.021>.
- Michelangeli, D.V., Toon, O.B., Haberle, R.M., Pollack, J.B., 1993. Numerical simulations of the formation and evolution of water ice clouds in the martian atmosphere. *Icarus* 100, 261–285.
- Millour, E. et al., 2008. The latest (version 4.3) Mars Climate Database. *LPI Contrib.* 1447, 9029+.
- Millour, E. et al., 2012. Mars Climate Database Version 5. In: *European Planetary Science Congress*, p. 302.
- Mitchell, D.L., Lillis, R.J., Lin, R.P., Connerney, J.E.P., Acuña, M.H., 2005. A global map of Mars' crustal magnetic field based on electron reflectometry. In: Mackwell, S., Stansbery, E. (Eds.), *Lunar Planet. Sci.* 36, 2366.
- Molina-Cuberos, G.J., Lichtenegger, H., Schwingenschuh, K., López-Moreno, J.J., Rodrigo, R., 2002. Ion-neutral chemistry model of the lower ionosphere of Mars. *J. Geophys. Res. (Planets)* 107, 5027. <http://dx.doi.org/10.1029/2000JE001447>.
- Molina-Cuberos, G.J., Witasse, O., Lebreton, J.P., Rodrigo, R., López-Moreno, J.J., 2003. Meteoric ions in the atmosphere of Mars. *Planet. Space Sci.* 51, 239–249. [http://dx.doi.org/10.1016/S0032-0633\(02\)00197-6](http://dx.doi.org/10.1016/S0032-0633(02)00197-6).
- Montmessin, F., Rannou, P., Cabane, M., 2002. New insights into martian dust distribution and water-ice cloud microphysics. *J. Geophys. Res.* 107 (E6), 5037. <http://dx.doi.org/10.1029/2001JE001520>.
- Montmessin, F., Forget, F., Rannou, P., Cabane, M., Haberle, R.M., 2004. Origin and role of water ice clouds in the Martian water cycle as inferred from a general circulation model. *J. Geophys. Res.* 109, E10004. <http://dx.doi.org/10.1029/2004JE002284>.
- Montmessin, F., Bertaux, J.L., Quémerais, E., Korablev, O., Rannou, P., Forget, F., Perrier, S., Fussen, D., Lebonnois, S., Reberac, A., Dimarellis, E., 2006. Subvisible CO₂ clouds detected in the mesosphere of mars. *Icarus* 183, 403–410.
- Montmessin, F. et al., 2007. Hyper-spectral imaging of convective CO₂ ice clouds in the equatorial mesosphere of Mars. *J. Geophys. Res.* 112. <http://dx.doi.org/10.1029/2007JE002944>.
- Montmessin, F., Forget, F., Bertaux, J.L., Spiga, A., Määttänen, A., 2011. Existence of supercold atmospheric layers in the martian mesosphere. In: *The Fourth International Workshop on the Mars Atmosphere: Modelling and Observation*, held 8–11 February, 2011, Paris, France, pp. 404–405. Scientific Committee: Forget, F., Allen, M., Desjean, M.C., Haberle, R. M., Head, J. W., Hollingsworth, J.L., Huot, J.P., Lefevre, F., Levine, J.S., Lewis, S.R., Lopez-Valverde, M.A., Montmessin, F., Rafkin, S., Read, P. L., Spiga, A., Witasse, O., and Wolff, M.J. Published online at <http://www-mars.lmd.jussieu.fr/paris2011/program.html>.
- Nesvorný, D., Jenniskens, P., Levison, H.F., Bottke, W.F., Vokrouhlický, D., Gounelle, M., 2010. Cometary origin of the zodiacal cloud and carbonaceous micrometeorites. Implications for hot debris disks. *Astrophys. J.* 713, 816–836. <http://dx.doi.org/10.1088/0004-637X/713/2/816>, arXiv:0909.4322.
- Noel, V., Pitts, M., 2012. Gravity wave events from mesoscale simulations, compared to polar stratospheric clouds observed from spaceborne lidar over the Antarctic Peninsula. *J. Geophys. Res. (Atmos.)* 117, 11207. <http://dx.doi.org/10.1029/2011JD017318>.
- Pandya, B.M., Haider, S.A., 2012. Meteor impact perturbation in the lower ionosphere of Mars: MGS observations. *Planet. Space Sci.* 63, 105–109. <http://dx.doi.org/10.1016/j.pss.2011.09.013>.
- Pätzold, M., Tellmann, S., Häusler, B., Hinson, D., Schaa, R., Tyler, G.L., 2005. A sporadic third layer in the ionosphere of Mars. *Science* 310, 837–839. <http://dx.doi.org/10.1126/science.1117755>.
- Rapp, M., Thomas, G.E., 2006. Modeling the microphysics of mesospheric ice particles: Assessment of current capabilities and basic sensitivities. *J. Atmos. Solar-Terr. Phys.* 68, 715–744. <http://dx.doi.org/10.1016/j.jastp.2005.10.015>.
- Rodin, A.V., Korablev, O.I., Moroz, V.I., 1997. Vertical distribution of water in the near-equatorial troposphere of Mars: Water vapor and clouds. *Icarus* 125, 212–229. <http://dx.doi.org/10.1006/icar.1996.5602>.
- Rohatschek, H., Horvath, H., 2010. Magneto-phosphoresis and mesospheric particles. *J. Geophys. Res. (Atmos.)* 115, 24208. <http://dx.doi.org/10.1029/2010JD014667>.
- Schofield, J.T. et al., 1997. The Mars Pathfinder Atmospheric Structure Investigation/Meteorology (ASI/MET) experiment. *Science* 278, 1752–1757.
- Scholten, F., Hoffmann, H., Määttänen, A., Montmessin, F., Gondet, B., Hauber, E., 2010. Concatenation of HRSC colour and OMEGA data for the determination and 3D-parameterization of high-altitude CO₂ clouds in the martian atmosphere. *Planet. Space Sci.* 58, 1207–1214. <http://dx.doi.org/10.1016/j.pss.2010.04.015>.
- Sefton-Nash, E., Teanby, N.A., Montabone, L., Irwin, P.G.J., Hurlley, J., Calcutt, S.B., 2013. Climatology and first-order composition estimates of mesospheric clouds from Mars Climate Sounder limb spectra. *Icarus* 222, 342–356. <http://dx.doi.org/10.1016/j.icarus.2012.11.012>.
- Smith, M.D., 2009. THEMIS observations of Mars aerosol optical depth from 2002–2008. *Icarus* 202, 444–452. <http://dx.doi.org/10.1016/j.icarus.2009.03.027>.
- Spiga, A., Forget, F., 2009. A new model to simulate the martian mesoscale and microscale atmospheric circulation: Validation and first results. *J. Geophys. Res.* 114. <http://dx.doi.org/10.1029/2008JE003242>, 2009+.
- Spiga, A., González-Galindo, F., López-Valverde, M.A., Forget, F., 2012. Gravity waves, cold pockets and CO₂ clouds in the martian mesosphere. *Geophys. Res. Lett.* 39, 2201. <http://dx.doi.org/10.1029/2011GL050343>.
- Spiga, A., Faure, J., Madeleine, J.B., Määttänen, A., Forget, F., 2013. Rocket dust storms and detached dust layers in the martian atmosphere. *J. Geophys. Res. (Planets)* 118, 746–767. <http://dx.doi.org/10.1002/jgre.20046>, arXiv:1208.5030.

- Thomas, G.E., 1991. Mesospheric clouds and the physics of the mesopause region. *Rev. Geophys.* 29, 553–575. <http://dx.doi.org/10.1029/91RG01604>.
- Tobie, G., Forget, F., Lott, F., 2003. Numerical simulation of the winter polar wave clouds observed by Mars Global Surveyor Mars Orbiter Laser Altimeter. *Icarus* 164, 33–49.
- Toon, O.B., Turco, R.P., Jordan, J., Goodman, J., Ferry, G., 1989. Physical processes in polar stratospheric ice clouds. *J. Geophys. Res.* 94, 11359–11380.
- Turco, R.P., Toon, O.B., Hamill, P., Whitten, R.C., 1981. Effects of meteoric debris on stratospheric aerosols and gases. *J. Geophys. Res.* 86, 1113–1128.
- Vehkamäki, H., Määttänen, A., Lauri, A., Napari, I., Kulmala, M., 2007. Technical note: The heterogeneous Zeldovich factor. *Atmos. Chem. Phys.* 7, 309–313.
- Vincendon, M., Pilorget, C., Gondet, B., Murchie, S., Bibring, J.P., 2011. New near-IR observations of mesospheric CO₂ and H₂O clouds on Mars. *J. Geophys. Res. (Planets)* 116, 0. <http://dx.doi.org/10.1029/2011JE003827>, arXiv:1103.3448.
- Warren, S.G., 1986. Optical constants of carbon dioxide ice. *Appl. Opt.* 25, 2650–2674. <http://dx.doi.org/10.1364/AO.25.002650>.
- Wiegert, P., Vaubaillon, J., Campbell-Brown, M., 2009. A dynamical model of the sporadic meteoroid complex. *Icarus* 201, 295–310. <http://dx.doi.org/10.1016/j.icarus.2008.12.030>.
- Withers, P., Mendillo, M., Hinson, D.P., Cahoy, K., 2008. Physical characteristics and occurrence rates of meteoric plasma layers detected in the martian ionosphere by the Mars Global Surveyor Radio Science Experiment. *J. Geophys. Res. (Space Phys.)* 113, 12314. <http://dx.doi.org/10.1029/2008JA013636>.
- Wood, S.E., 1999. Nucleation and Growth of CO₂ ice Crystals in the Martian Atmosphere. Ph.D. Thesis, Univ. of Calif. Los Angeles.
- Wood, S.E., Baker, M.B., Calhoun, D., 2001. New model for the vapor growth of hexagonal ice crystals in the atmosphere. *J. Geophys. Res.* 106, 4845–4870. <http://dx.doi.org/10.1029/2000JD900338>.